POLITECNICO
MILANO 1863

DIPARTIMENTO DI MECCANICA

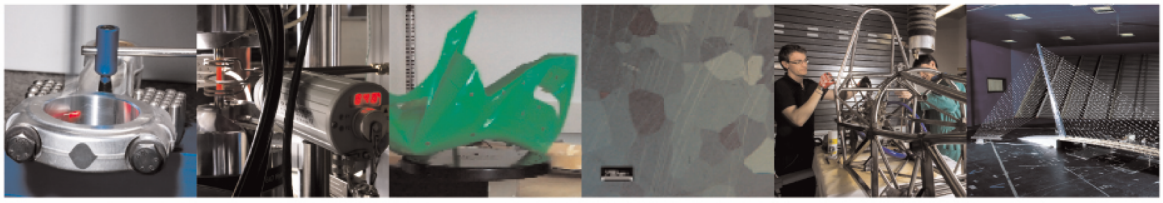

# Evaluation of hydrogen trapping and diffusion in two cold worked crmo(v) steel grades by means of the electrochemical hydrogen permeation technique

Peral L. B.;Amghouz Z.;Colombo C.;Fernandez-Pariente I.

This is a post-peer-review, pre-copyedit version of an article published in Theoretical and Applied Fracture Mechanics. The final authenticated version is available online at: https://doi.org/10.1016/j.tafmec.2020.102771



DIPARTIMENTO DI MECCANICA ■ POLITECNICO DI MILANO
via G. La Masa, 1 ■ 20156 Milano ■ EMAIL (PEC): pecmecc@cert.polimi.it
http://www.mecc.polimi.it
Rev. 0

# EVALUATION OF HYDROGEN TRAPPING AND DIFFUSION IN TWO COLD WORKED CrMo(V) STEEL GRADES BY MEANS OF THE ELECTROCHEMICAL HYDROGEN PERMEATION TECHNIQUE

L.B.Peral[1], Z.Amghouz[1], C.Colombo[2] and I.Fernández-Pariente[1]

[1]Department of Material Science and Metallurgical Engineering, Polytechnic School of Engineering of Gijón, University of Oviedo, Spain

[2]Department of Mechanical Engineering, Polytechnic of Milan, Italy

Corresponding author: luisborjapm@gmail.com (L.B.Peral)

## Abstract

Hydrogen diffusion kinetics, which is influenced by the hydrogen trapping and de-trapping phenomena within the steel microstructure, plays an important role on the behaviour of steel components under hydrogen environments. Hence, the complex interaction between hydrogen atoms and steel microstructure must be analyzed in order to discuss the impact of hydrogen on the structural damage.

Quenched and tempered low-alloy ferritic steels from the Cr-Mo family, with and without vanadium, have been subjected to different plastic deformation ratios by cold rolling. Dislocation densities have been determined by the analysis of the peak broadening on X-Ray diffractograms. Hydrogen diffusion kinetics was characterized by means of hydrogen permeation transients. In addition, binding energies between hydrogen atoms and microstructure were also determined using thermal desorption analysis (TDA). The analysis of the results highlights the influence of dislocations density and vanadium carbides on the hydrogen diffusion kinetics. In the 2.25Cr1Mo steel grade, hydrogen apparent diffusion coefficient decreased after the cold-work due to the increase in the density of traps (mainly related to dislocation core, $\Delta E_{TL}$~55-60kJ/mol). Nevertheless, after 10% of plastic deformation, apparent diffusion coefficient 'saturates' according to the 'plateau' determined in the dislocation density evolution at higher deformation levels. Due to the vanadium addition (+0.31%), hydrogen apparent diffusion coefficient was notably reduced (compared to that obtained in the V-free steel grade). Hydrogen trapping and diffusion are the result of the interplay between vanadium carbides ($\Delta E_{TL}$~35kJ/mol) and dislocation core.

**Keywords**: hydrogen permeation, CrMoV steel, cold-work, X-Ray Diffraction, dislocation density, vanadium carbides.

## 1 Introduction

Hydrogen embrittlement (HE) is a phenomenon responsible for premature failure of steel structures leading to the total loss of the structural integrity [1]. For the impending new hydrogen society, vessels and pipelines used to store and transport hydrogen must be able to provide a safe service during long periods of time in direct contact with hydrogen under high internal pressure, being then essential to ensure good resistance to hydrogen

embrittlement (HE). Although Cr-Mo and Cr-Mo-V steel grades are commonly used in these type of facilities [1], it is necessary to understand the complex embrittlement phenomena that take place when hydrogen diffuses into these metallic components submitted to static and cyclic mechanical loads under hydrogen environments. In this regard, hydrogen diffusion through a steel wall is dominated by specific microstructural sites, called traps, which have hydrogen binding energies higher than regular interstitial sites (lattice sites). Accordingly, the definition of the different hydrogen states in steel (lattice hydrogen, reversible trapped and irreversible trapped hydrogen) is necessary to discuss the impact of hydrogen on damage [2, 3]. Hence, three type of sites (lattice, reversible and irreversible sites) can be distinguished in the steel microstructure as a function of the trapping energy. Although hydrogen reversibility process within the steel microstructure depends on the concentration and temperature, irreversible trapping character can be assumed when detrapping energy is higher than 30 kJ/mol [2, 4-7]. Figure 1 illustrates the detrapping activation energy, '$\Delta E_{TL}$', for each trapping site according to literature data.

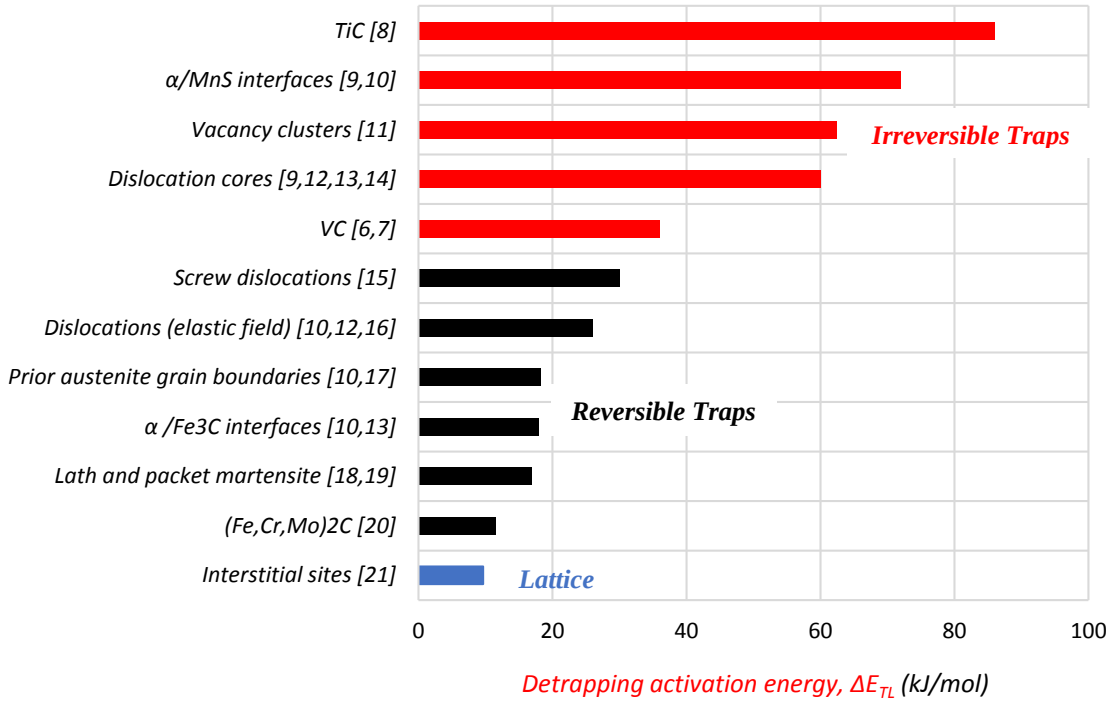


*Figure 1. Detrapping activation energy, $\Delta E_{TL}$, for each scale of trapping sites*

Weak and medium energy trapping sites (reversible traps) can contribute to delay hydrogen transport towards the fracture process zone. Nevertheless, these trapping sites can act as a reservoir of diffusible hydrogen when they are saturated and no lattice hydrogen is available. Taking into account that hydrogen embrittlement process is dependent on the time, stress gradient (hydrostatic stress) and temperature [3, 4, 22-24], diffusible hydrogen (lattice hydrogen and reversible trapped hydrogen) can redistribute (trapping/de-trapping) within the steel microstructure during the service life of the structural components. Competition between trapping and de-trapping phenomena (diffusible hydrogen redistribution) is illustrated in Figure 2. Indeed, de-trapped hydrogen atoms, motivated by the existing high hydrostatic stress, can diffuse toward a

damage process zone (notch area, Figure 2), promoting hydrogen embrittlement when a critical hydrogen concentration is reached, following the Oriani's theory [25] according to equation 1, where: '$C_{H\text{-}notch}$' is the hydrogen concentration in the vicinity of the notch, '$H_D$' the diffusible hydrogen content (lattice and reversible hydrogen), '$\sigma_H$' is the hydrostatic stress developed in the notch region, '$V_H$' is the partial molar volume of hydrogen in BCC Fe ($V_H$=2.1·10$^{-6}$ m$^3$/mol), 'R' the gas constant and 'T' is the testing temperature.

$$C_{H\text{-}notch} = H_D \exp\left(\frac{\sigma_H \cdot V_H}{R \cdot T}\right) \qquad (1)$$

On the other hand, irreversible hydrogen traps (high energy traps, see Figure 1) homogeneously distributed within the steel microstructure can notably contribute to delay hydrogen diffusion towards the mentioned damage process zone. Therefore, hydrogen accumulation on the process zone might be limited, contributing to improve the steel behavior in presence of internal hydrogen [3, 5, 23, 24]. At this respect, the addition of vanadium to chromium-molybdenum steels to estimulate the precipitation of vanadium carbides during the tempering was demonstrated to be a good practice in order to fight against hydrogen embrittlement [3, 5, 7]. Different authors have proved that vanadium carbides act as strong hydrogen traps [6, 7]. This highlights that the hydrogen states (i.e. type of hydrogen traps: weak, medium and high energy traps) are key factors for the hydrogen damage process, underlying the important role that microstructural units play on hydrogen embrittlement process.

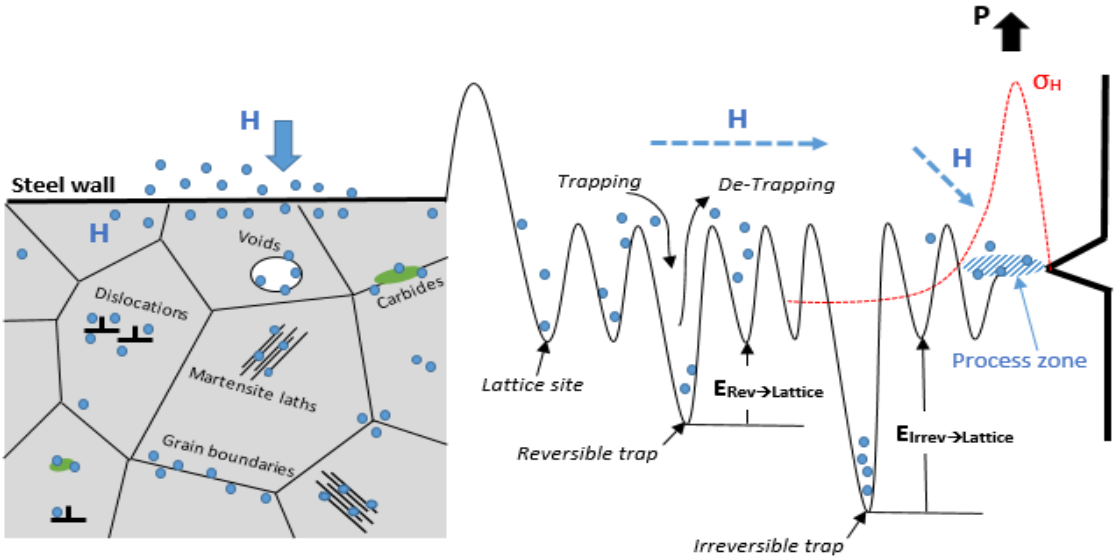


*Figure 2. Hydrogen diffusion ($H_D$=lattice+reversible hydrogen) towards the damage process zone motivated by the existing high hydrostatic stress ($\sigma_H$) near the notch area*

Therefore, in order to study the interaction of hydrogen atoms with the steel microstructure, the purpose of this paper is to analyse hydrogen diffusion and trapping processes through two quenched and tempered low alloy steel grades (2.25Cr1Mo and 2.25Cr1MoV). The novelty of the work is addressed to the focus on the effect of plastic deformation rate (dislocations density) on hydrogen diffusion kinetics of different industrial steel grades, evaluating at the same time, the vanadium carbides effect (precipitated during the tempering treatments) on the hydrogen trapping and diffusion.

## 2 Experimental procedure

### 2.1 Materials, applied heat treatments and cold rolling process

Two different low-alloyed ferritic steels from the Cr-Mo family have been selected in this study, with or without vanadium. Table 1 shows the chemical composition of the steel grades. Pressure vessels employed in the petrochemical industry for hydrogen services are commonly manufactured with Cr-Mo-V steel grades. In order to achieve a good combination of strength and toughness, these grades of steel are commonly used in quenched and tempered conditions [1].

| Steel grade | C | Mn | Si | Cr | Mo | Ni | V |
|---|---|---|---|---|---|---|---|
| 2.25Cr1Mo | 0.143 | 0.563 | 0.157 | 2.23 | 1.00 | 0.090 | - |
| 2.25Cr1MoV | 0.150 | 0.520 | 0.086 | 2.27 | 1.06 | 0.186 | 0.31 |

*Table 1. Chemical composition of 2.25Cr1Mo and 2.25Cr1MoV steels (weight %)*

Heat treatments were applied on blocks of 50x40x20 $mm^3$. The sequence of heat treatments and the yield strength ($\sigma_y$) are shown in Table 2.

| Steel grade | Heat treatment sequences | $\sigma_y$ (MPa) |
|---|---|---|
| 2.25Cr1Mo | 940ºC/3h+ water quenched + 690ºC/30h tempered | 430 |
| 2.25Cr1MoV | 925ºC/90min+ water quenched + 720ºC/3h tempered | 567 |

*Table 2. Applied heat treatments on the steel blocks (50x40x20 $mm^3$)*

After performing heat treatments, samples of 1.3, 1.2, 1.1 and 1 mm of thickness ($t_0$) were cut from the treated steel blocks. Then, samples were cold-rolled using a TD 140 Maquijoy rolling mill. The process is illustrated in Figure 3.

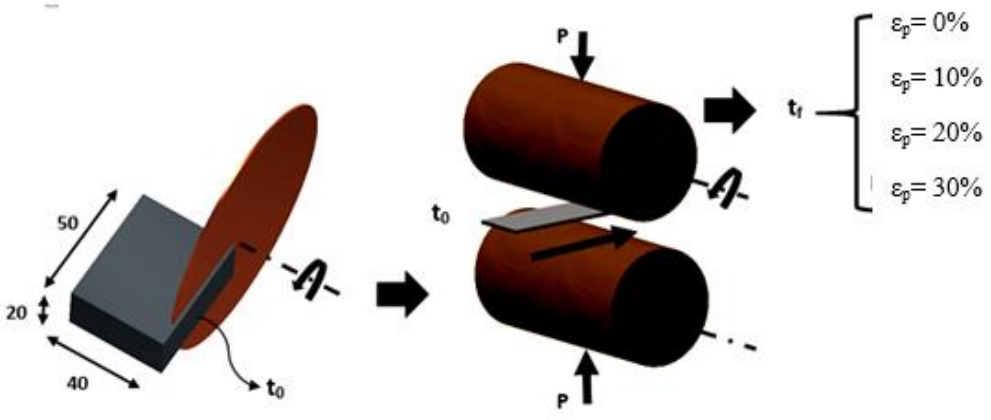


*Figure 3. Sample preparation. (a) Cutting operation and (b) Cold rolling process*

After the cold rolling process, the final thickness ($t_f$) was of 1 mm for all the plates and consequently, the plastic deformation ratio was 30, 20 and 10%, respectively (Table 3). The corresponding levels of plastic deformation, $\varepsilon_p$, were calculated according to equation 2, where: '$t_0$' and '$t_f$' are respectively, the initial and final thickness of the rolled specimens.

$$\varepsilon_p = \frac{t_0 - t_f}{t_0} \cdot 100 \text{ (in \%)} \qquad (2)$$

| Initial thickness, $t_0$ (mm) | Final thickness, $t_f$ (mm) | $\varepsilon_p$ (%) |
|---|---|---|
| 1.3 | 1.0 | 30 |
| 1.2 | 1.0 | 20 |
| 1.1 | 1.0 | 10 |
| 1.0 | 1.0 | 0 |

*Table 3. Plastic deformation ratio applied on both grades of steel by means of the cold-rolling process*

After the rolling process, the cold-rolled steel sheets were cut in square pieces of 20 mm length. Finally, they were polished with SiC up to 600 grit and then, they were cleaned in an ultrasonic bath with acetone in order to perform the electrochemical hydrogen permeation tests.

## 2.2 Microstructure characterization

### 2.2.1 Scanning Electron Microscopy and Transmission Electron Microscopy

Microstructural characterization was carried out by means of a SEM-Jeol-JSM5600 microscope using an acceleration voltage of 20 kV. Previously, the samples were ground and finally polished with diamond paste of 1µm and etched with Nital-2%.

On the other hand, TEM analysis was performed for prepared samples of the heat treated V-free and V-added grades. The transmission electron microscopy studies (TEM, HRTEM, BF-STEM and EDX analysis) was carried out using a JEOL JEM-2100F field-emission transmission electron microscope operating at an accelerating voltage of 200 kV and equipped with an ultrahigh resolution pole piece that provides a point resolution higher than 0.19 nm. The samples were prepared for viewing in the TEM. First, the samples were sectioned (thickness c.a. 1mm) with a diamond disk cutter (Struers Minitom) and then thinned to approx. c.a. 200 µm. Afterwards, the ion-thinning of ~2 x 4mm$^2$ specimen was performed on Precision Ion Polishing System (PIPS™ model 691 from Gatan), at an Ar-ion beam acceleration voltage of 4 keV and incident angle of 10º, then gentle milling at 0.5keV until perforation of the specimen occurs. Finally, SOLARUS 950 Advanced Plasma Cleaning System was used to clean sample surface before observation.

### 2.2.2 Microhardness Analysis

After applying the different plastic deformation ratios ($\varepsilon_p$), microhardness measurements were conducted by using a Buehler Micromet 2100 tester, applying a load of 200 gf during 15s. The diagonals of the indentation marks were measured by optical microscope.

### 2.2.3 Residual Stresses

Residual stresses were measured using a Stresstech 3000-G3R X-ray diffractometer. The Kα chromium wavelength (0.2291 nm) was employed onto the {211} ferrite/martensite planes under a 2Θ angle of 156.4º. The residual stress was determined using the $\sin^2\psi$ technique by means of equation 3 [26].

$$\sigma_{\emptyset} = \left(\frac{E}{1+\nu}\right)_{(hkl)} \left(\frac{1}{d_{\emptyset 0 hkl}}\right) \left(\frac{\partial d_{\emptyset\psi hkl}}{\partial \sin^2\psi}\right) \qquad (3)$$

Where: 'E' and 'v' are the elastic modulus and Poisson coefficient of the 2.25Cr1Mo(V) steel grades in the measured crystallographic plane, taken as 211000 MPa and 0.3 respectively; 'd' is the interplanar distance of the selected diffraction plane (hkl), '$\psi$' the tilt angle and 'Ø' the angle in the sample plane. The detection of the diffraction peak was carried out at nine positions of the tilt angle, between -45 and +45º, using an exposure time of 40 seconds in each position. The working parameters used for the measurement of residual stresses conducted after the cold-rolling are shown in Table 4.

| Measurement mode | Modified χ |
|---|---|
| Maximum voltage (kV) | 30 |
| Exposure time (s) | 40 |
| Tilt $\psi$ (º) | 9 points between -45°/+45° |
| Noise reduction | Parabolic |
| Filter of the $K_\alpha$ radiation | Vanadium |
| Maximum intensity (mA) | 6.7 |
| Collimator diameter (mm) | 1 |
| Goniometric rotation (measurement direction) Ø (º) | 0 |
| Peak adjustment | Pseudo-Voigt |

*Table 4. Working parameters used for residual stress measurements*

### 2.2.4 Dislocation density

After the cold-rolling process, dislocation density, $\rho$, in the steel sheets ($\varepsilon_p$=0%, $\varepsilon_p$=10%, $\varepsilon_p$=20% and $\varepsilon_p$=30% for each grade of steel with and without vanadium) was experimentally measured by using the full width half maximum (FWHM) according to the Williamson-Hall method [27].

The measurements were carried out using the aforementioned X-Ray diffractometer Stresstech 3000-G3R with Chromium Cr $K_\alpha$ radiation at 30 kV and 6.7 mA.

'FWHM' parameter was determined in the different 2Θ (°) positions corresponding to the martensite/ferrite diffraction planes:

$$\{211\}_{2\Theta=156.4^\circ},\ \{200\}_{2\Theta=106.1^\circ} \text{ and } \{110\}_{2\Theta=69^\circ}$$

Experimental data were analyzed using the Williamson-Hall equation (equation 4) in the diffraction planes (2Θ).

$$FWHM_{corrected}\ \frac{\cos(\Theta)}{\lambda} = \frac{k_s}{D} + 2\varepsilon\ \frac{\sin(\Theta)}{\lambda} \qquad (4)$$

Where: '$k_s$' is a shape factor that has been taken to equal 0.9 [28], 'Θ' is the diffraction angle, 'λ' the x-ray wave-length (0.229 nm for Chromium), 'D' the average particle size and '$FWHM_{corrected}$' the corrected total full width half maximum.

According to this method, the dislocation density,$\rho$, was calculated using the equation 5, where: 'k' is a constant that takes the value of 14.4 for Body Centered Cubic metals [29], 'b' represents the Burgers vector (b=0.248 nm, [29]) and 'ε' can be calculated from the slope of $FWHM_{corrected}\cdot\cos(\Theta)/\lambda$ versus $\sin(\Theta)/\lambda$ plot, according to equation 4.

$$\rho = k\cdot\left(\frac{\varepsilon}{b}\right)^2 \qquad (5)$$

Instrumental effect must be taken into account. For it, an estimation of the instrumental broadening ($FWHM_{instrumental}$) must be done to correct the initial width ($FWHM_{measured}$) of the different peaks in order to avoid the broadening caused by fine grain sizes [30]. Thus, the $FWHM_{corrected}$ avoiding the strain caused by fine grain sizes can be expressed according to equation 6.

$$FWHM^2_{corrected} = FWHM^2_{measured} - FWHM^2_{instrumental} \quad (6)$$

### 2.3 Hydrogen Electrochemical Permeation Experiments

The instrumentation of electrochemical hydrogen permeation was composed of an electrolytic cell with two compartments similar to Devanathan and Stachurski cell [31]. Figure 4 displays the experimental setup of the electrochemical permeation test employed in this study. A circular area of approximately 1 $cm^2$ was exposed to the solution and the electrochemical tests were conducted at room temperature (~20°C). Two hydrogen permeation tests were carried out on each sample state (from $\varepsilon_p$=0% to $\varepsilon_p$=30%) for both grades of steel.

Hydrogen atoms are generated on one side of the steel membrane (the entry side) and the diffusing hydrogen atoms are oxidized on the other side (the exit side). Accordingly, the current density (J) on the anodic side (hydrogen flow rate) was continuously recorded using an Ivium PocketSTAT potentiostat.

The cathodic side of the sample, corresponding to the hydrogen entry side, was galvanostatically polarized at a constant current density of 1 $mA/cm^2$ using a 2 mol L $H_2SO_4$ + 0.25 g/l of $AS_2O_3$ solution (pH~1). The electrochemical reactions occurring on the steel surface during cathodic polarization correspond to the hydrogen evolution reaction [32] composed by an initial electrochemical adsorption (Volmer domain, V) and an electrochemical desorption stage at higher cathodic polarization (Heyrovsky domain, H), as can be seen in Figure 4 . Hydrogen generation was conducted under 0.001 $A/cm^2$ (1 $mA/cm^2$). This current density was enough to ensure that hydrogen available in the solution, $H^+$, is reduced and partially adsorbed on the steel surface, until hydrogen diffuses along the steel thickness, so that its arrival can be registered as an evolution of the anodic current on the exit side [5, 24].

At the exit side, the samples were electrolytically coated with palladium [33, 34] prior to the permeation test to get the significant hydrogen permeation current density. The exit side contained 0.1 mol/L NaOH solution (pH~12) and was potentiostatically polarized at a constant potential of -50 mV versus a silver/silver-chloride (Ag/Ag-Cl) reference electrode. The detection side was previously maintained at this potential during 1800 seconds to stabilize the anodic current with approximately 0.1 $\mu A/cm^2$ [35].

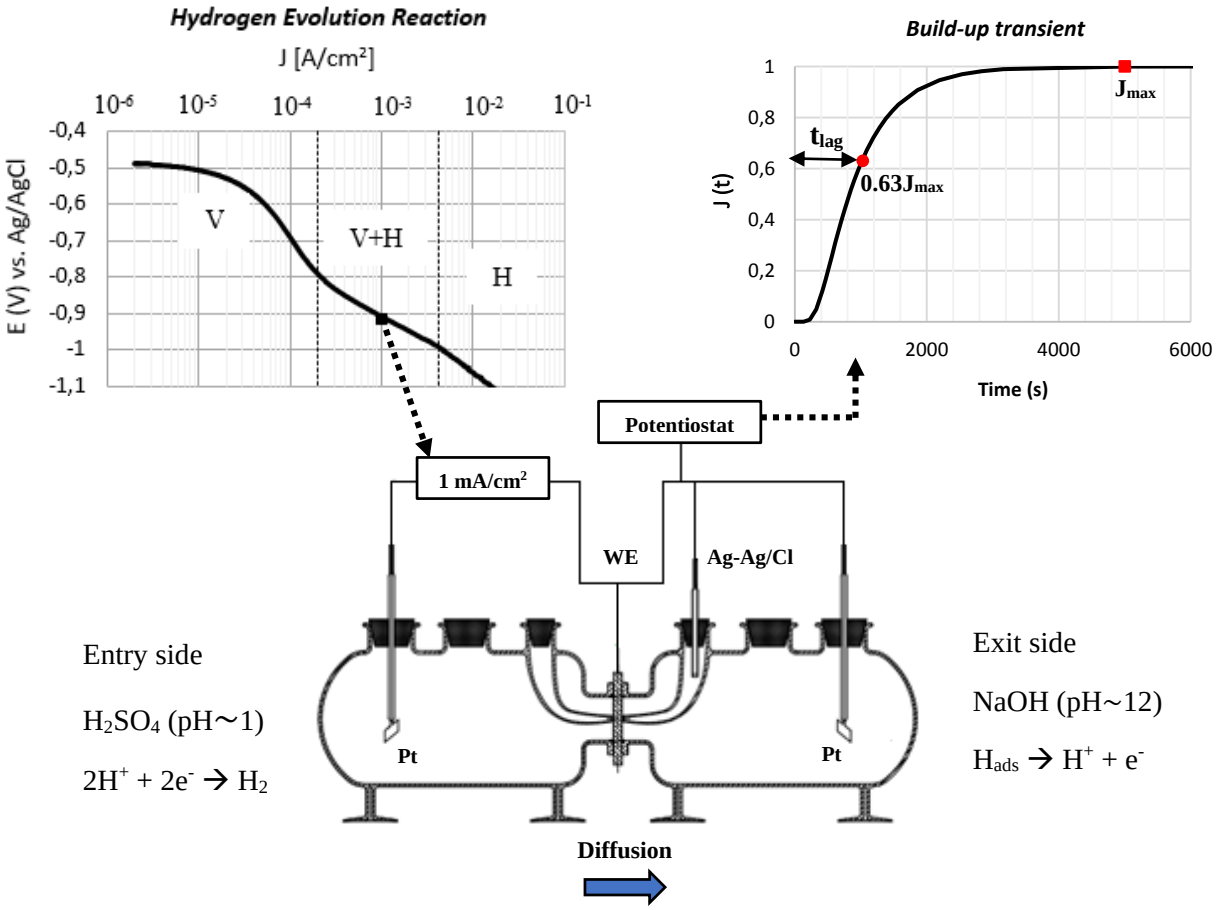


*Figure 4. Devanathan-Stachurski cell. WE: working electrode (steel sample). Cathodic polarization corresponding to the hydrogen evolution reaction for 2.25Cr1Mo(V) steel grades in 2 mol L $H_2SO_4$ + 0.25 g/l of $AS_2O_3$ solution (pH~1).*

To calculate the apparent diffusion coefficient ($D_{app}$), the 'time lag' method derived from Fick´s second law can be considered [35] according to equation 7.

$$D_{app} = \frac{L^2}{6 \cdot t_{lag}} \quad (7)$$

Where 'L' is the thickness of the sample and '$t_{lag}$' is the 'time lag' when $J=0.63J_{max}$, being 'J' the measured permeation current density and '$J_{max}$' the permeation current density corresponding to the steady state. The concentration of the subsurface, '$C_{app}$', that corresponds to the concentration of hydrogen at the cathodic side, can be estimated by equation 8 [35, 36], where '$M_H$' is the molar mass of hydrogen (1 g/mol), 'F' the Faraday constant (96485 C/mol) and '$\rho_{Fe}$' the iron density ($7.87 \cdot 10^6$ g/m$^3$). The apparent permeability ($P_{app}$) is defined according to equation 9.

$$C_{app} = \frac{J_{max} \cdot M_H \cdot L}{D_{app} \cdot F \cdot \rho_{Fe}} \quad (8)$$

$$P_{app} = C_{app} \cdot D_{app} \quad (9)$$

On the other hand, mathematical models proposed by McNabb and Foster [37] and later discussed by Kumnick and Johnson [38] can be used to determine the density of traps ($N_T$) in the microstructure steel through the direct application of the values of the

diffusivity and the concentration of the subsurface by means of equation 10, where: '$N_A$' is Avogadro´s constant ($6.022 \cdot 10^{23}$ $mol^{-1}$) and '$D_{Lattice}$' is the hydrogen diffusivity in the steel lattice.

$$N_T = \frac{C_{app}}{3} \cdot \left(\frac{D_{Lattice}}{D_{app}} - 1\right) \cdot N_A \qquad (10)$$

To estimate the lattice diffusion coefficient ($D_{Lattice}$), the discharge phase (after switching-off the cathodic current) can be used. According to Zakroczymski model [39], in the initial part of the discharge curve, where $1 \geq J/J_{max} \geq 0.9$, desorption of the lattice diffusible hydrogen prevails and this part of the curve is well described by the theoretical Fick´s law (equation 11).

$$\frac{dC}{dt} = D\frac{d^2C}{dx^2} \qquad (11)$$

Supposing that the hydrogen subsurface concentration is constant [36, 39], the diffusion process can be described according to equation 12. This equation represents the transport of hydrogen atoms where the steel membrane is supposed to be free of trap sites, if the experimental data adjustment is evaluated in the range where $1 \geq J(t)/J_{max} \geq 0.9$. Hence, theoretical lattice diffusivity can be determined by means of equation 12 and 13.

$$\frac{J(t)}{J_{max}} = 1 - \frac{2}{\sqrt{\pi \cdot \tau}} \sum_{n=0}^{\infty} \exp\left(-\frac{(2n+1)^2}{4\tau}\right) \qquad (12)$$

$$\text{Where: } \tau = \frac{D_{Lattice} \cdot t}{L^2} \quad (1 \geq J/J_{max} \geq 0.9) \qquad (13)$$

According to this, the complete decay can be used to quantify the lattice hydrogen and also the reversible trapped hydrogen [36, 40]. Figure 5 shows as an example, the experimental desorption curve on the exit side.

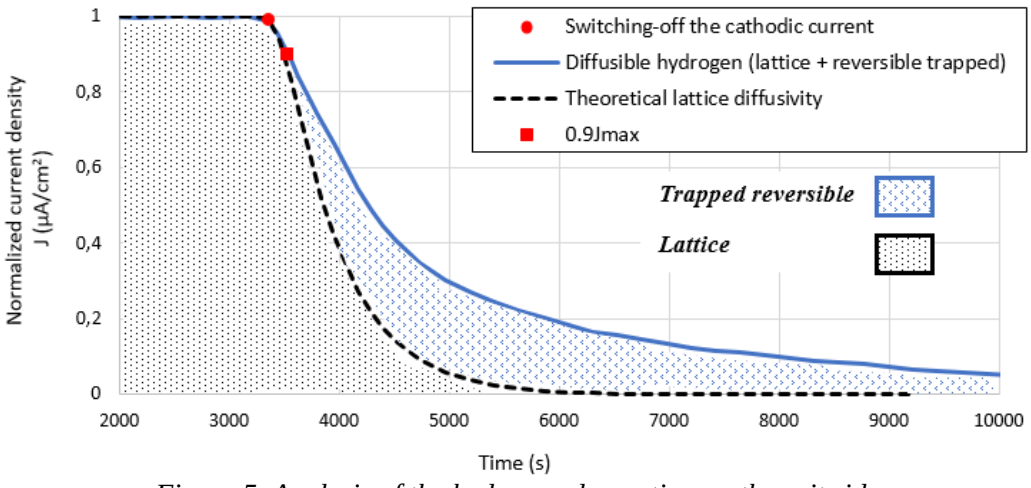


*Figure 5. Analysis of the hydrogen desorption on the exit side*

The area, 'A', in $\mu A \cdot s/cm^2$, defined between experimental and theoretical lattice diffusivity, corresponds to the amount of reversible trapped hydrogen ($C_{rev}$) in the steel microstructure. This area can be converted in 'ppm' of hydrogen using the equation 14.

$$C_H = A \cdot \frac{M_H}{F \cdot L \cdot p_{Fe}} \qquad (14)$$

According to equation 15, it is possible to estimate the amount of irreversible trapped hydrogen ($C_{irrev}$) by supposing that, when a palladium layer has been deposited on the exit side, hydrogen distribution into the steel membrane is not homogeneous and it corresponds to a linear profile approximated by $<C> \approx C_{app}/2$ [39, 40].

$$C_{irrev} = <C> - C_{Lattice} - C_{rev} \quad (15)$$

On the other hand, the mobility of dissolved hydrogen within the steel microstructure, taking into account the trapping effect, can be analyzed using Oriani's theory [41] and Krom-Bakker trap model [42]. Considering equilibrium between diffusible and trapped hydrogen, the trapping energy, '$\Delta E_T$', can be determined using equation 16, where '$\theta_L$' is the occupancy of lattice sites (equation 17) and '$\theta_T$' is the occupancy of trap sites (equation 18). '$K_b$' is the Boltzmann constant ($8.62 \cdot 10^{-5}$ eV/K) and 'T' is the temperature (in K).

$$\frac{1}{\theta_L}\left(\frac{\theta_T}{1-\theta_T}\right) = \exp(k_t) \text{ with } k_t = \left(-\frac{\Delta E_T}{K_B \cdot T}\right) \quad (16)$$

$$\theta_L = \frac{C_{Lattice}}{N_L} \quad (17)$$

$$\theta_T = \frac{C_T}{N_T} \quad (18)$$

Hence, equation 16 can be written as a function of the hydrogen states according to equation 19 where the number of lattice sites per unit of volume, '$N_L$', was set to of $5.2 \cdot 10^{29}$ sites/$m^3$ for tetrahedral interstitial sites in the ferrite lattice [43].

$$\ln\frac{C_T}{C_L} = -\ln\frac{N_L}{N_T - C_T} - \frac{\Delta E_T}{K_B \cdot T} \quad (19)$$

Detrapping activation energy ($\Delta E_{TL}$) for hydrogen moving from a lattice site to a trapping site might be determined using equation 20 where '$\Delta E_{Lattice}$' is the activation energy for moving from a lattice site to an adjacent lattice site (Figure 6). Hydrogen lattice diffusion coefficient can be related to '$\Delta E_{Lattice}$' by means of a pre-exponential factor ($D_0$) according to equation 21 and 22. '$D_{0app}$' was taken as $1.25 \cdot 10^{-6}$ $m^2/s$ for quenched and tempered martensite microstructure [36].

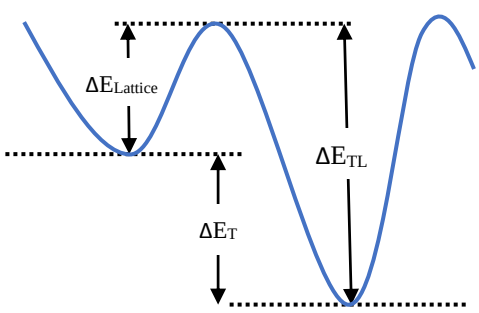


*Figure 6. Schematic view of energy relations in hydrogen microstructure system*

$$\Delta E_{TL} = \Delta E_T + \Delta E_{Lattice} \quad (20)$$

$$D_{Lattice} = D_0 \exp\left(\frac{\Delta E_{Lattice}}{K_B \cdot T}\right) \quad (21)$$

$$D_0 = \frac{D_{0app} \cdot D_{Lattice}}{D_{app}} \quad (22)$$

## 2.4 Activation energy estimation by Thermal Desorption Analysis (TDA)

In order to complete the analysis carried out by means of hydrogen permeation tests, in a second step, detrapping activation energies from the different microstructural traps were determined using cylindrical samples manufactured from the same steel blocks. In this case, cold-plastic deformation was not applied. Cylindrical samples with a diameter of 10 mm and a length of 30 mm (weight ≈20 grams) were pre-charged with gaseous hydrogen in a high-pressure reactor, manufactured in accordance with the ASTM G146 standard [44]. Hydrogen precharge was conducted under conditions described in Table 5.

| Pressure (MPa) | Temperature (ºC) | Time (hours) |
|---|---|---|
| 19.5 | 450 | 21 |

*Table 5. Hydrogen precharge conditions*

After the maintenance time (21 hours), a cooling phase of 1 hour, until a temperature of 85ºC (keeping the hydrogen pressure at 19.5 MPa to minimize hydrogen departure) was always used. The hydrogen pre-charged specimens were removed from the reactor and rapidly immersed in liquid nitrogen (at -196ºC), where they were kept until the moment of testing, in order to limit hydrogen losses.Thereupon, to study the hydrogen trapping effect in the mentioned steel grades, different heating rates (3600, 2400, 1800, 1200, 800ºC/h) were applied by using a hydrogen analyzer LECO DH603 for determining trapping energies, specifically detrapping activation energies, '$\Delta E_{TL}$', as depicted in Figure 6. Before starting the different measures, each cylindrical sample was cleaned in an ultrasonic bath with acetone for 5 minutes, and then carefully dried using cold air.

Assuming that the release of hydrogen from a trapping site is a thermally activated process, the hydrogen evolution rate from trapping sites can be written according to Equation 23, proposed by Kissinger [45].

$$\frac{dX_H}{dt} = A\,(1\text{-}X_H)^n \exp\left(-\frac{\Delta E_{TL}}{R\cdot T}\right) \qquad (23)$$

Here: 'n' is the reaction order (usually taken as one), '$X_H$' is the fraction of hydrogen evolved from a trapping site characterized by a detrapping activation energy and 'A' is a constant. Kissinger's equation is transferred to TDA assuming temperature as the new dependent variable. Hence, when a hydrogen-charged specimen is heated at a uniform rate, '$\phi_i$', such that $T=T_0+\phi_i \cdot t$, a hydrogen peak, related to the detrapping activation energy, is detected at a certain temperature, '$T_{p_i}$'. Substituting this heating uniform rate in expression 23, the following equation is obtained:

$$\ln\left(\frac{\phi_i}{T_{p_i}^2}\right) = -\frac{\Delta E_{TL}}{R}\left(\frac{1}{T_{p_i}}\right) + \ln\left(A\frac{R}{\Delta E_{TL}}\right) \qquad (24)$$

Equation 24 can be linearly fitted by plotting $\ln(\phi_i/T_{pi}^2)$ versus $1/T_p$. Hence, detrapping activation energy can be determined by measuring the change in peak temperature ($T_{pi}$) with heating rate ($\phi_i$) according to equation 25.

$$\frac{\partial\left[\mathrm{Ln}\left(\frac{\phi_i}{T_{p_i}^2}\right)\right]}{\partial\left(\frac{1}{T_{p_i}}\right)} = -\frac{\Delta E_{TL}}{R} \qquad (25)$$

## 3 Results

### 3.1 Microstructure characterization

The obtained microstructures of the 2.25Cr1Mo and 2.25Cr1MoV steels after the heat treatments described in Table 2 are shown in Figure 7. They correspond to tempered martensite. The steel grades were composed of martensite laths, with similar average thickness, around 1µm. Prior austenite grain boundary was around 25 µm. The profuse carbides precipitation that takes place during the tempering stage can be also seen. Fe-Cr-Mo mixed carbides, belonging to $M_7C_3$, $M_2C$ and $M_{23}C_6$ were identified in the V-free steel grade by means of the TEM analysis, whereas V-added grade evidenced mixed carbides of V and Mo with a finer particle size (MC submicrometric carbides, 10-30nm), which will be shown later.

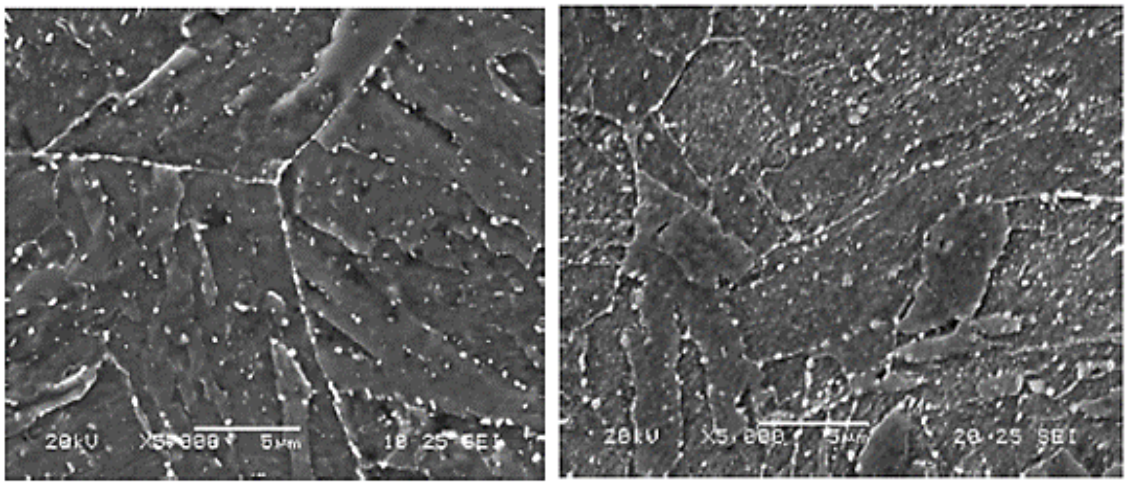

*(a)* *(b)*

*Figure 7. SEM analysis. (a) 2.25Cr1Mo_$\varepsilon_p$=0%, (b) 2.25Cr1MoV_$\varepsilon_p$=0%*

### 3.2 Vickers microhardness, residual stresses and dislocation density evolution

Vickers microhardness (HV) and residual stresses level depending on the applied plastic deformation ratio are shown in Figure 8(a) and Figure 8(b), respectively. According to these results, it can be clearly appreciated that Vickers Hardness increased on both grades of steel as plastic deformation ratio increased. Regarding the internal residual stresses field, residual stresses increased after the cold-work operation and values in the range of -150 MPa were determined (Figure 8b).

To estimate the density of dislocations, Figure 8(c) and (d) show the variation of $FWHM_{corrected} \cdot \cos(\Theta)/\lambda$ as a function of the $\text{sen}(\Theta)/\lambda$ obtained for the different plastic deformation ratios using the Williamson method, according to equation 4. Hence, the slope, '$2\varepsilon$', can be determined in order to estimate the dislocation density ($\rho$) by means of the equation 5. Dislocation density evolution is shown in Figure 8(e). Therefore, on both steel grades with and without vanadium, dislocation density increased after cold-work until reaching an asymptotic value when 10% of plastic deformation was reached.

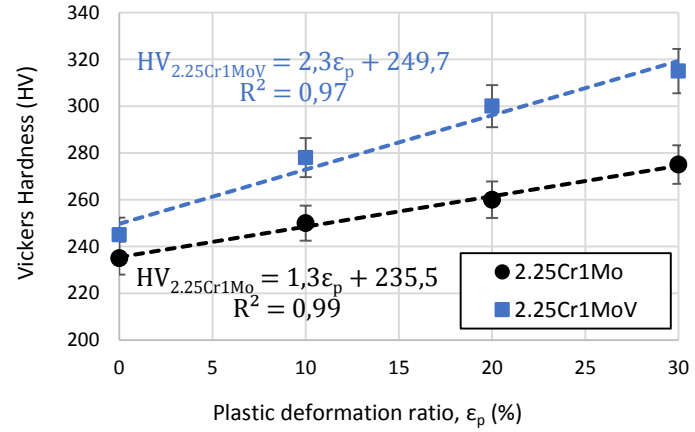


*(a)*

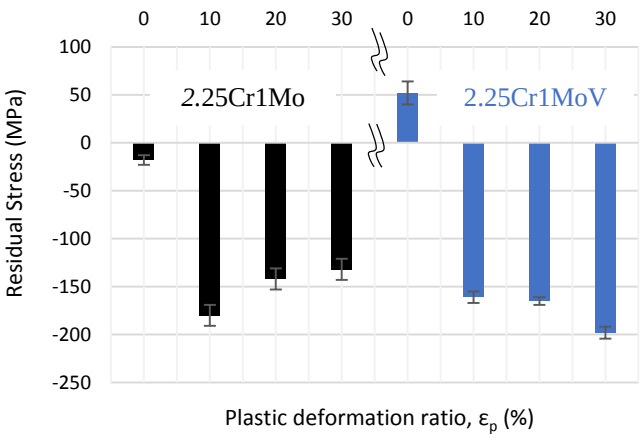


*(b)*

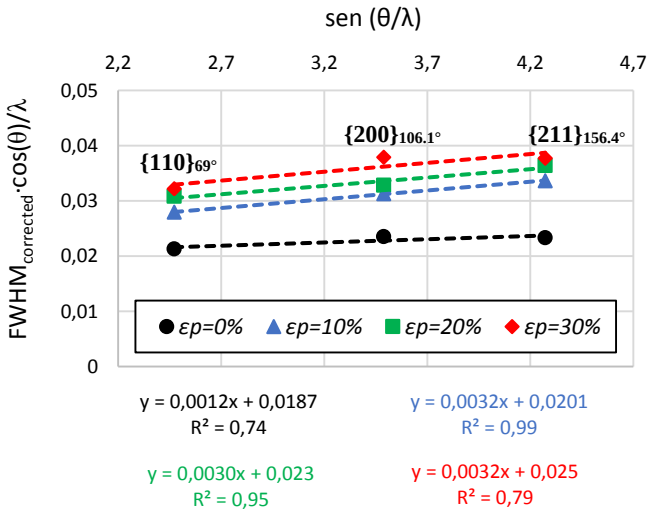


*(c) 2.25Cr1Mo (V-free)*

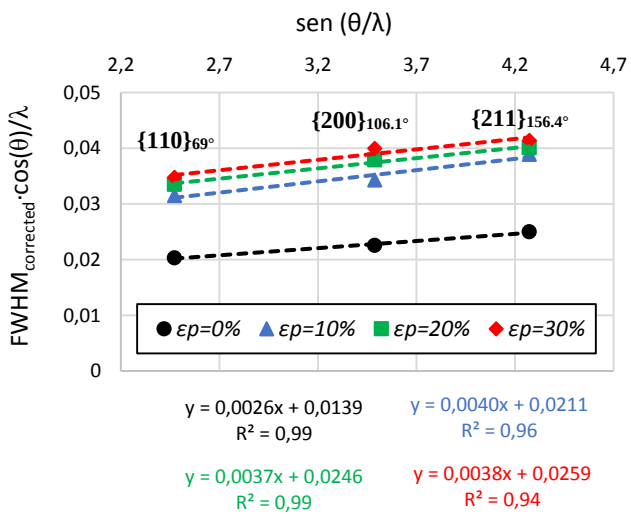


*(d) 2.25Cr1MoV (V-added)*

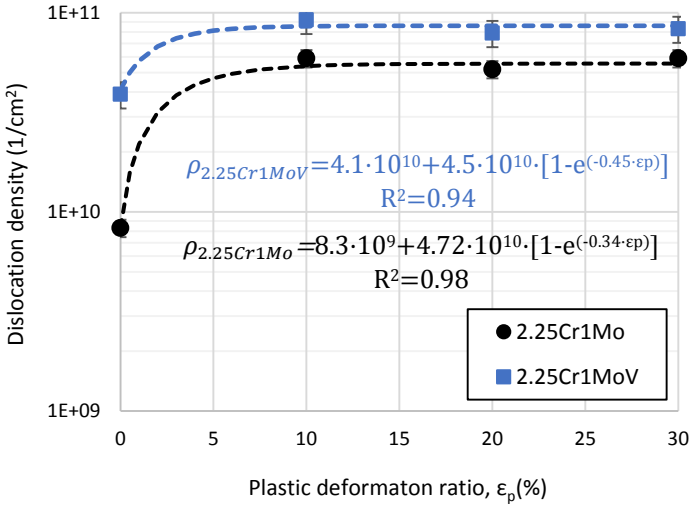


*(e)*

| Steel grade | $\varepsilon_p$ (%) | 2ε (slope, equation 4) | $\rho$ ($cm^{-2}$) (equation 5) |
|---|---|---|---|
| **2.25Cr1Mo** | 0 | 0.0012 | $8.3 \cdot 10^9$ |
| | 10 | 0.0032 | $5.9 \cdot 10^{10}$ |
| | 20 | 0.0030 | $5.2 \cdot 10^{10}$ |
| | 30 | 0.0032 | $5.9 \cdot 10^{10}$ |
| **2.25Cr1MoV** | 0 | 0.0026 | $3.9 \cdot 10^{10}$ |
| | 10 | 0.0040 | $9.2 \cdot 10^{10}$ |
| | 20 | 0.0037 | $7.9 \cdot 10^{10}$ |
| | 30 | 0.0038 | $8.3 \cdot 10^{10}$ |

*Figure 8. (a) Micro-hardness evolution. (b) Residual stresses evolution. (c),(d) and (e) Dislocation density estimation using Williamson method*

### 3.3 Hydrogen Electrochemical Permeation Tests

#### 3.3.1 Permeation tests in 2.25Cr1Mo steel grade

Figure 9(a) shows the build-up permeation transients corresponding to the cold rolled 2.25Cr1Mo steel grade under the different plastic deformation ratios ($\varepsilon_p$) together with the 2.25Cr1Mo grade without plastic deformation ($\varepsilon_p$=0%). Figure 9(b) shows the decay transient once that hydrogen generation current density is switched-off on the cathodic side.

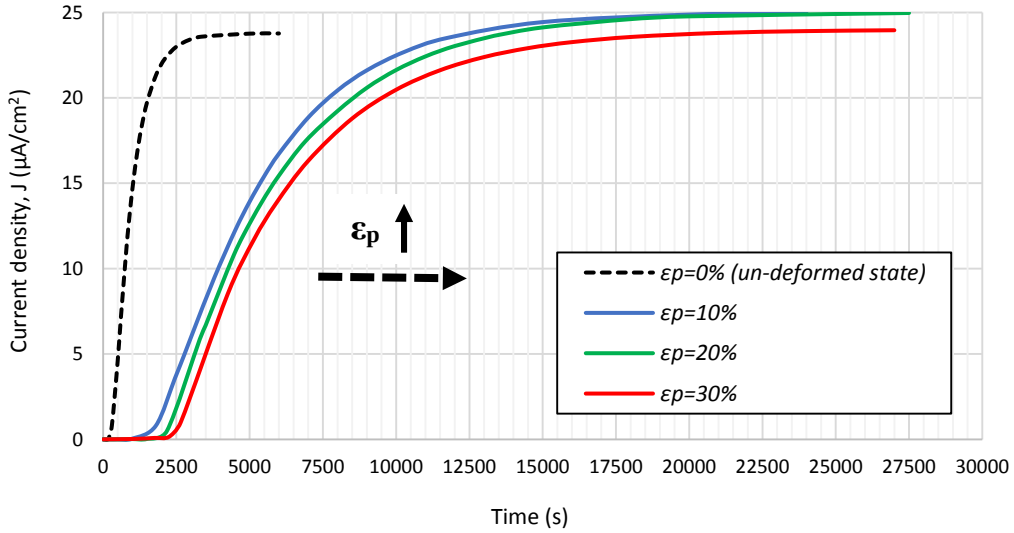


*(a)*

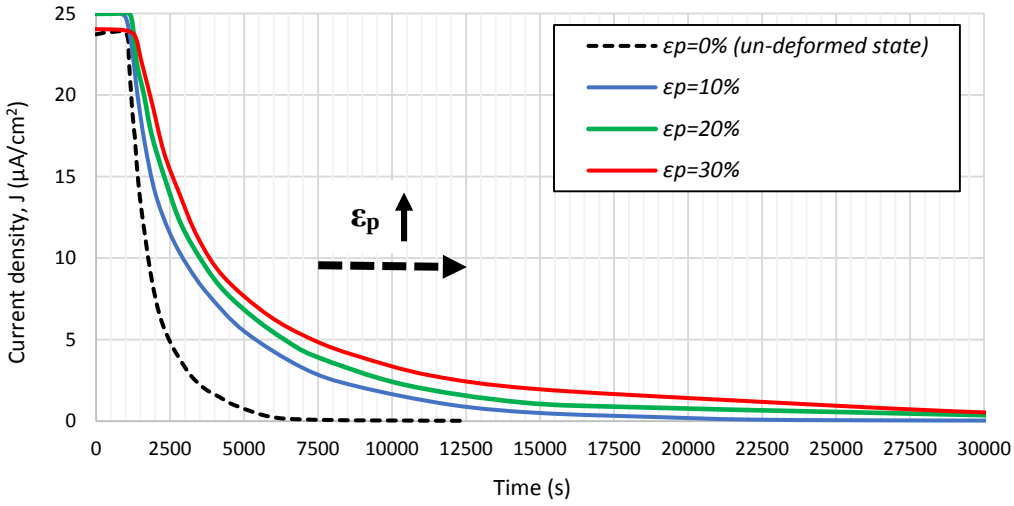


*(b)*

*Figure 9. Hydrogen permeation results on 2.25Cr1Mo steel grade. (a) Build-up transient. (b) Decay transient (after switching-off the cathodic current)*

From Figure 9 can be seen that the steady-state hydrogen current density is practically constant independently on the applied plastic deformation ratio [46, 47]. Another observation is the growing delay of the permeation transient with the increase of the plastic deformation ratio, as also revealed in [46, 47].

Table 6 displays the results obtained from the electrochemical permeation tests, where: '$\varepsilon_p$' is the applied plastic deformation ratio, '$C_{app}$' the hydrogen apparent concentration, '$P_{app}$' the hydrogen permeability, '$t_{lag}$' is the time necessary to attain the 63% of '$J_{max}$' (hydrogen flux corresponding to steady-state), '$D_{app}$' is the hydrogen apparent diffusion coefficient, '$D_{Lattice}$' is the hydrogen lattice diffusivity and '$N_T$' is the density of traps for hydrogen in the steel microstructure.

| $\varepsilon_p$ (%) | $C_{app}$ (ppm) | $P_{app}$ (molH/m·s) | $t_{lag}$ (s) | $D_{app}$ [$t_{lag}$] ($m^2/s$) | $D_{Lattice}$ ($m^2/s$) | $N_T$ (sites/$m^3$) |
|---|---|---|---|---|---|---|
| 0 | 1.90 | $1.22 \cdot 10^{-9}$ | 1000 | $1.70 \cdot 10^{-10}$ | $6.00 \cdot 10^{-10}$ | $3.80 \cdot 10^{24}$ |
| 10 | 11.0 | $1.28 \cdot 10^{-9}$ | 5500 | $3.00 \cdot 10^{-11}$ | $1.20 \cdot 10^{-10}$ | $2.52 \cdot 10^{25}$ |
| 20 | 12.0 | $1.28 \cdot 10^{-9}$ | 6100 | $2.73 \cdot 10^{-11}$ | $1.00 \cdot 10^{-10}$ | $2.51 \cdot 10^{25}$ |
| 30 | 12.0 | $1.23 \cdot 10^{-9}$ | 6300 | $2.65 \cdot 10^{-11}$ | $9.00 \cdot 10^{-11}$ | $2.25 \cdot 10^{25}$ |

*Table 6. Data obtained from the hydrogen electrochemical permeation tests in the 2.25Cr1Mo steel grade*

As an example, Figure 10 shows the theoretical data adjustment ($1 \geq J/J_{max} \geq 0.9$) performed to estimate the lattice diffusion coefficient in the case of the 2.25Cr1Mo_$\varepsilon_p$=10% steel grade.

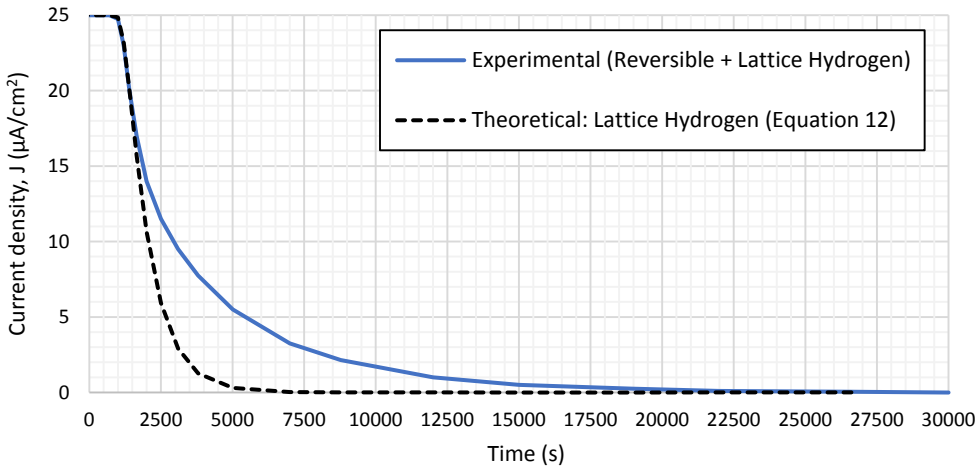


*Figure 10. Decay transient (after switching-off the cathodic current). 2.25Cr1Mo_$\varepsilon_p$=10% ($D_{Lattice}=1.20 \cdot 10^{-10}$ $m^2/s$, in Table 6)*

As can be seen in Table 6, the apparent hydrogen diffusion coefficient ($D_{app}$) decreased around 6 times ($D_{app_{\varepsilon p=0\%}}=D_{app_{\varepsilon p=10\%}}$x6) when a plastic deformation ratio of 10% was applied, while the apparent hydrogen concentration ($C_{app}$) increased. This phenomenon can be explained due to the increase in the density of traps ($N_T$) after applying a plastic deformation rate of 10% ($N_{T_{\varepsilon p=10\%}}=N_{T_{\varepsilon p=0\%}}$x7). After this deformation ratio, the density of traps ($N_T$) barely varied and consequently, the apparent diffusion coefficient remained practically constant.

As can be seen in Figure 11, the lattice diffusion coefficient ($D_{Lattice}$) determined in the 2.25Cr1Mo steel under the different plastic deformation ratios gave values in the range of $10^{-10}$ $m^2/s$, which are lower than the values of the lattice diffusivity of hydrogen in pure iron ($D_{Fe\alpha} \sim 10^{-8}$-$10^{-9}$ $m^2/s$) [36, 48]. This fact can be justified by the effect of solute atoms (Cr-Mo) and by the presence of internal compression stresses [49] mainly caused by the cold rolling process (Figure 8b). Besides, cold-work seems to affect regular diffusion

sites, contributing to decrease the lattice hydrogen diffusivity. The distortion of the lattice may occasion elastic fields near the regular lattice diffusion sites and may interfere with the hydrogen mobility. This fact was also reported in [50].

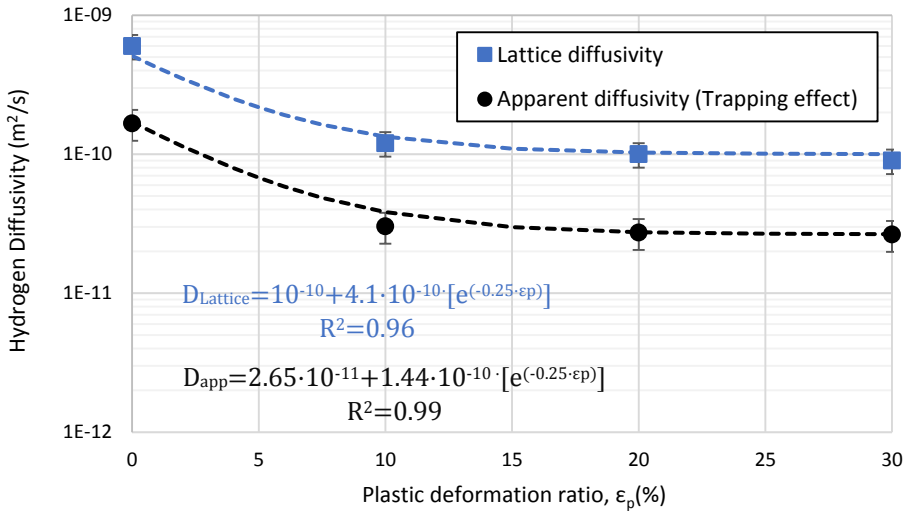


*Figure 11. Effect of the plastic deformation ratio on the hydrogen diffusivity of the 2.25Cr1Mo steel grade.*

It is likely that dislocation density might be considered as the main type of trap that dominates the hydrogen diffusion kinetics in this grade of steel (V-free) under these plastic deformation ratios, where the estimated dislocation density, in the range of $10^9$-$10^{10}$ $cm^{-2}$, is not negligible as was also corroborated by TEM analysis (Figure 12).

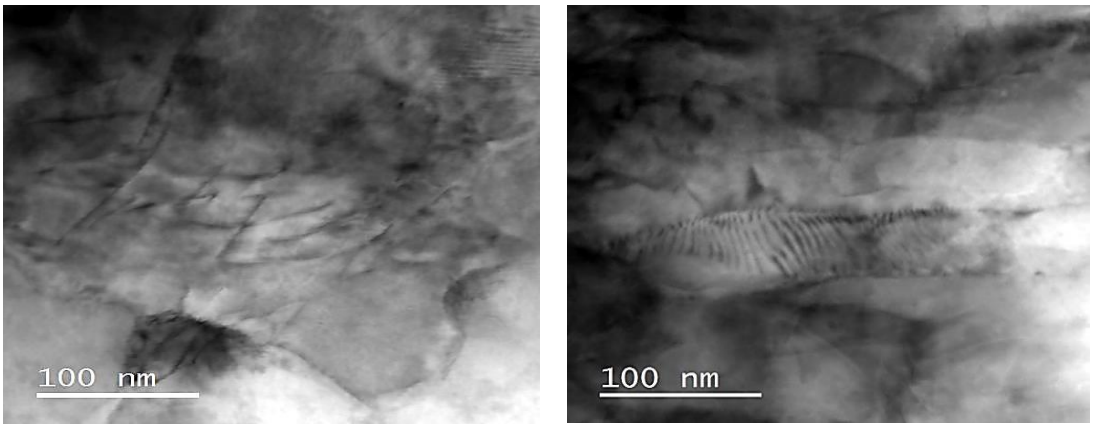


*Figure 12. TEM micrograph showing dislocation lines in the cold-deformed 2.25Cr1Mo_$\varepsilon_p$=30% sample. $\rho = 5.9 \cdot 10^{10} cm^{-2}$*

Therefore, it is worth underlying that the trapping density ($N_T$) increased (in the regime 1) and, after 10% of plastic deformation ratio, trapping density stabilized (in the regime 2) following the trend marked by the dislocation density evolution as can be seen in Figure 13. Consequently, the opposite effect was observed in the apparent hydrogen diffusion coefficient evolution (Figure 14). The apparent diffusion coefficient ($D_{app}$) decreased in the 'regime 1' as trapping density (i.e. dislocation density) increased while '$D_{app}$' stabilized in the 'regime 2' due to the stabilization of the number of trapping sites.

In the un-deformed state ($\varepsilon_p$=0%), the energy '$\Delta E_{Lattice}$' is equal to 0.23eV (equation 21) and '$\Delta E_T$' from equation 19 is equal to 0.34eV. Consequently, the detrapping activation

energy has been estimated to be $\Delta E_{TL} = \Delta E_T + \Delta E_{Lattice} \sim 0.57$eV (~55 kJ/mol, $\varepsilon_p$=0%). These values have the same order of magnitude of [36, 38]. '$\Delta E_{Lattice}$' slightly increased after cold-work, presumably due to the distortion induced near the regular lattice sites by means of the rolling process. '$\Delta E_{Lattice}$' values in the range of 0.27eV and '$\Delta E_T$' values in the range of 0.33eV were determined (with $\Delta E_{TL} \sim 0.6$eV, ~58kJ/mol). These trapping energies ($\Delta E_{TL}$) which can be related to dislocation core [9, 12-14, 20], contribute to corroborate the strong influence of dislocation density on hydrogen trapping. Due to its strong hydrogen binding energy, dislocation core might be characterized to be non-diffusible hydrogen trapping sites, i.e. irreversible trapping sites [4].

Some authors reported for pure-iron values of '$\Delta E_{Lattice}$' in the range between 0.1 [21] and 0.2eV [51], lower than our data. Hence, the aforementioned implication of lattice distortion (cold-work) and solute atoms (Cr-Mo) on hydrogen diffusion is reinforced.

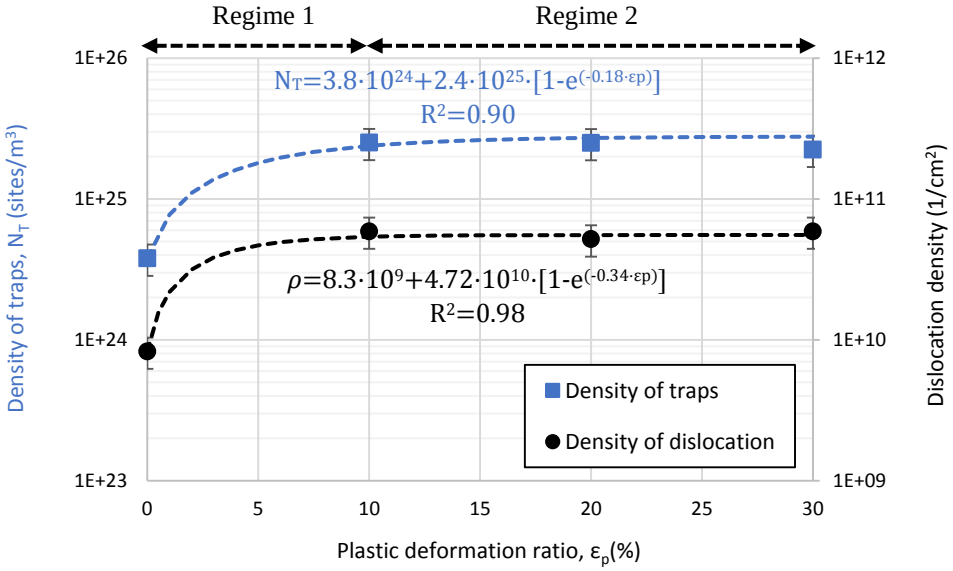


*Figure 13. Effect of plastic deformation rate on the hydrogen trapping of the 2.25Cr1Mo steel grade*

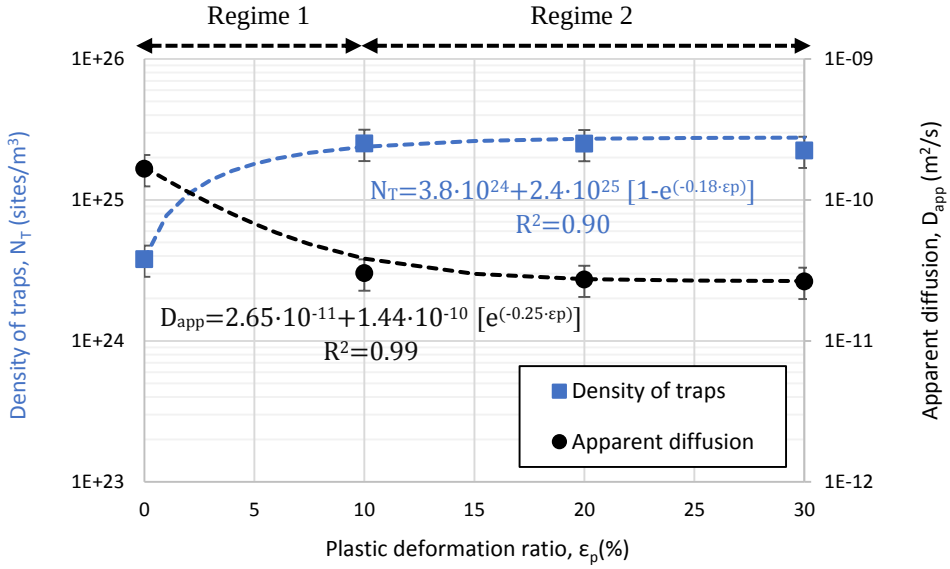


*Figure 14. Effect of plastic deformation rate on the hydrogen diffusion kinetics of the 2.25Cr1Mo steel grade*

As mentioned, the complete decay of the desorption step is sensitive to hydrogen release. The amounts of lattice hydrogen ($C_{Lattice}$), reversible hydrogen ($C_{rev}$) and irreversible trapped hydrogen ($C_{irrev}$) are given in Table 7. The same table gives the '$\Delta E_{TL}$' values.

| $\varepsilon_p$ (%) | $C_{Lattice}$ (ppm) | $C_{rev}$ (ppm) | $C_{irrev}$ (ppm) | $\Delta E_{TL}$ (eV) |
|---|---|---|---|---|
| 0 | 0.15 | 0.34 | 0.46 | 0.57 |
| 10 | 0.50 | 1.00 | 4.00 | 0.60 |
| 20 | 0.55 | 1.05 | 4.40 | |
| 30 | 0.60 | 1.10 | 4.20 | |

*Table 7. Hydrogen states in the 2.25Cr1Mo steel grade*

In the un-deformed state ($\varepsilon_p$=0%), the percentage of irreversible trapped hydrogen ($\%C_{irrev}$= ($C_{irrev}$/<C>) was around 48%, while the estimated diffusible hydrogen percentage was around 52% ($\%C_{diffusible}$= ($C_{Lattice}$+$C_{rev}$)/<C>). After applying cold-plastic deformation, hydrogen contents notably increased (Figure 15) in comparison to the un-deformed state ($\varepsilon_p$=0%) due mainly to the increase in the number of hydrogen traps. However, in the regime 2 (after 10% of plastic deformation), trapped hydrogen tends to a constant value following the evolution marked by the density of traps (i.e. dislocation density evolution, Figure 13) mainly associated to dislocation core ($\Delta E_{TL}$~0.57-0.60eV). In this regime, the most of hydrogen remained irreversibly trapped ($\%C_{irrev}$~70%) in the steel microstructure. This supports our initial hypothesis, i.e. that the hydrogen trapping is mainly due to dislocations core, acting as irreversible trapping sites for hydrogen. It is worth nothing that, although the trapping energy ($\Delta E_{TL}$) determined was similar in all states (Figure 15), the percentage of irreversible hydrogen was higher (48→70%) after cold-work due to the increase (from $\varepsilon_p$=0% to $\varepsilon_p$=10%) in the total density of hydrogen strong traps (mainly related to dislocation core).

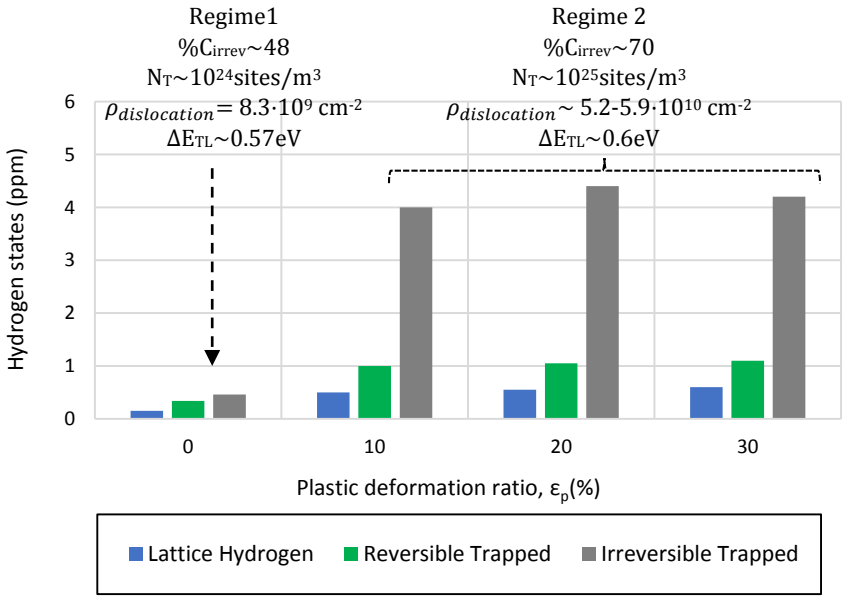


*Figure 15. Evolution of irreversible, reversible trapped and lattice hydrogen as a function of the plastic deformation ratio. 2.25Cr1Mo steel grade.*

### 3.3.2 Permeation tests in 2.25Cr1MoV steel grade

After the V-free, also the V-added steel grade was studied under the same plastic deformation ratios ($\varepsilon_p$). Figure 16(a) and (b) show the build-up permeation transients and the decay transients as a function of the plastic deformation rate, while Table 8 gives the results obtained from the electrochemical hydrogen permeation tests.

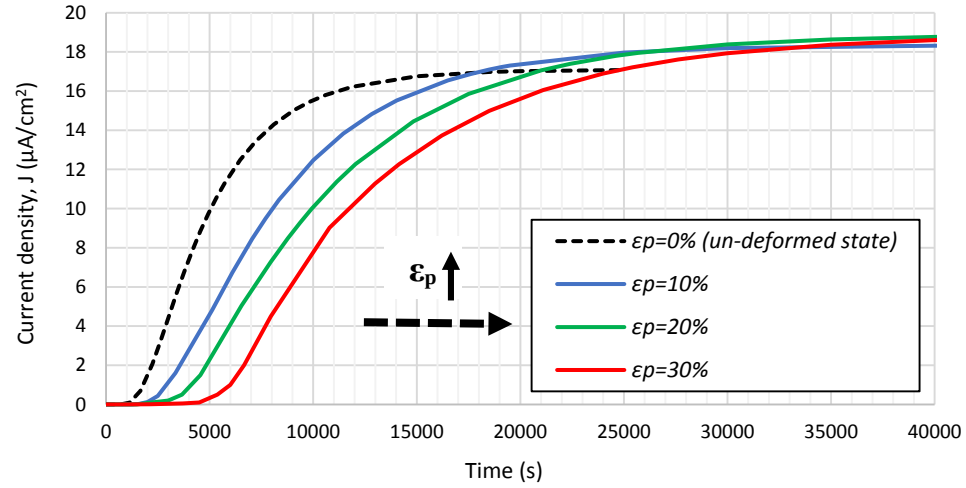


*(a)*

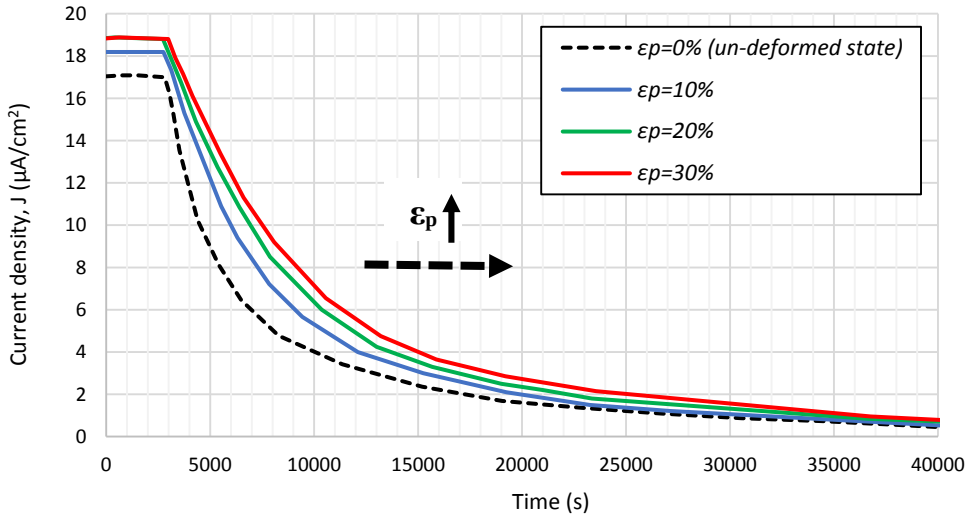


*(b)*

*Figure 16. Hydrogen permeation results on 2.25Cr1MoV steel grade. (a) Build-up transient. (b) Decay transient (after switching-off the cathodic current)*

Figure 16 shows a delay of the permeation transient as plastic deformation ratio ($\varepsilon_p$) is increased, while steady-state hydrogen current density remained practically constant independent of the plastic deformation ratio. The apparent diffusion coefficient ($D_{app}$) determined in the $\varepsilon_p$=30% deformed state was around 2.5 times lower than the one estimated without plastic deformation ($\varepsilon_p$=0%-state). The apparent diffusivity decreased from $3.1 \cdot 10^{-11}$ $m^2/s$ (un-deformed state, $\varepsilon_p$=0%) to $1.2 \cdot 10^{-11}$ $m^2/s$ ($\varepsilon_p$=30%-state), as it can be seen in Table 8. Regarding the plasticity effect on the lattice diffusivity, $D_{Lattice}$ also decreased after cold-work presumably due to the distortion created near the regular lattice sites a cause of the cold-work [50]. Figure 17 shows the lattice and the apparent hydrogen diffusivity evolution depending on the plastic deformation ratio.

As mentioned in the V-free steel grade, the decrease observed in the apparent hydrogen diffusivity ($D_{app}$) is explained due to the increase in the density of traps ($N_T$, Table 8) obtained after applying cold-work. According to this, trapping density ($N_T$) increased from $2.3 \cdot 10^{25}$ sites/m$^3$ (without plastic deformation, $\varepsilon_p$=0%) to $8.5 \cdot 10^{25}$ sites/m$^3$ when a plastic deformation ratio of 30% ($\varepsilon_p$=30%) was applied. Hence, trapping density estimated after applying 30% of plastic deformation was around 3.5 times higher than the one estimated in the $\varepsilon_p$=0%, un-deformed state. According to this fact, the apparent hydrogen concentration ($C_{app}$) increased from 7.2 ppm ($\varepsilon_p$=0%) to 20 ppm ($\varepsilon_p$=30%). Nevertheless, it is important to note that the apparent permeability ($P_{app}$) remained practically constant independently of the introduced plastic deformation ratio, as given in Table 8.

| $\varepsilon_p$ (%) | $C_{app}$ (ppm) | $P_{app}$ (molH/m·s) | $t_{lag}$ (s) | $D_{app}$ [$t_{lag}$] (m$^2$/s) | $D_{Lattice}$ (m$^2$/s) | $N_T$ (sites/m$^3$) |
|---|---|---|---|---|---|---|
| 0 | 7.2 | $8.8 \cdot 10^{-10}$ | 5320 | $3.1 \cdot 10^{-11}$ | $1.6 \cdot 10^{-10}$ | $2.3 \cdot 10^{25}$ |
| 10 | 13.0 | $9.4 \cdot 10^{-10}$ | 9000 | $1.9 \cdot 10^{-11}$ | $8.5 \cdot 10^{-11}$ | $3.7 \cdot 10^{25}$ |
| 20 | 17.0 | $9.7 \cdot 10^{-10}$ | 11400 | $1.5 \cdot 10^{-11}$ | $8.0 \cdot 10^{-11}$ | $6.0 \cdot 10^{25}$ |
| 30 | 20.0 | $9.0 \cdot 10^{-10}$ | 13400 | $1.2 \cdot 10^{-11}$ | $8.0 \cdot 10^{-11}$ | $8.5 \cdot 10^{25}$ |

*Table 8. Data obtained from the hydrogen electrochemical permeation tests in the 2.25Cr1MoV steel grade*

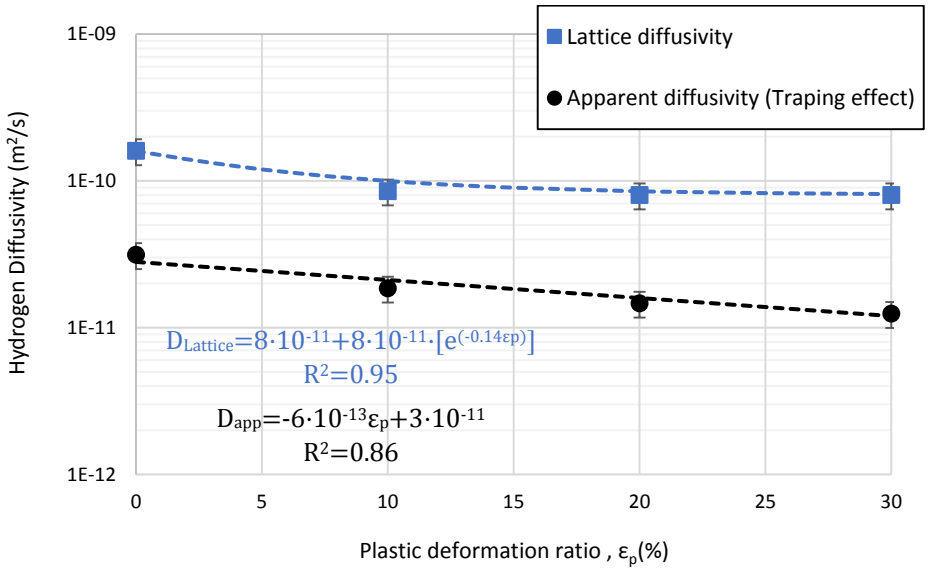


*Figure 17. Effect of the plastic deformation rate on the hydrogen diffusivity of the 2.25Cr1MoV steel grade*

In the $\varepsilon_p$=0% un-deformed state, the energy '$\Delta E_{Lattice}$' was around 0.27eV, while '$\Delta E_T$' was equal to 0.32eV and the detrapping activation energy ($\Delta E_{TL}$) for moving from a lattice site to a trapping site is $\Delta E_{TL} = \Delta E_T + \Delta E_{Lattice} \sim 0.59$eV. After cold-work, '$\Delta E_{Lattice}$' values around 0.28eV and '$\Delta E_T$' values around 0.31eV were determined (with $\Delta E_{TL} \sim 0.59$eV). As in the case of the V-free steel grade, these detrapping activation energies can be associated to dislocation core [9, 12-14, 20].

Although dislocation density (i.e. dislocation core) displayed an asymptotic value after reaching 10% of plastic deformation, the trapping density ($N_T$) continued to increase as

plastic deformation ratio also increased (Figure 18). This fact suggests that another type of microstructural trap (presumably vanadium carbides) might also play an important role on the hydrogen trapping, as it will be discussed latter by means of the TDA analysis. It is important to remember that this effect was not previously observed in the V-free grade under the same plasticity ratios because of trapping density stabilized around 10% of cold-plastic deformation, following the dislocation density evolution, as previously shown in Figure 13 and Figure 14.

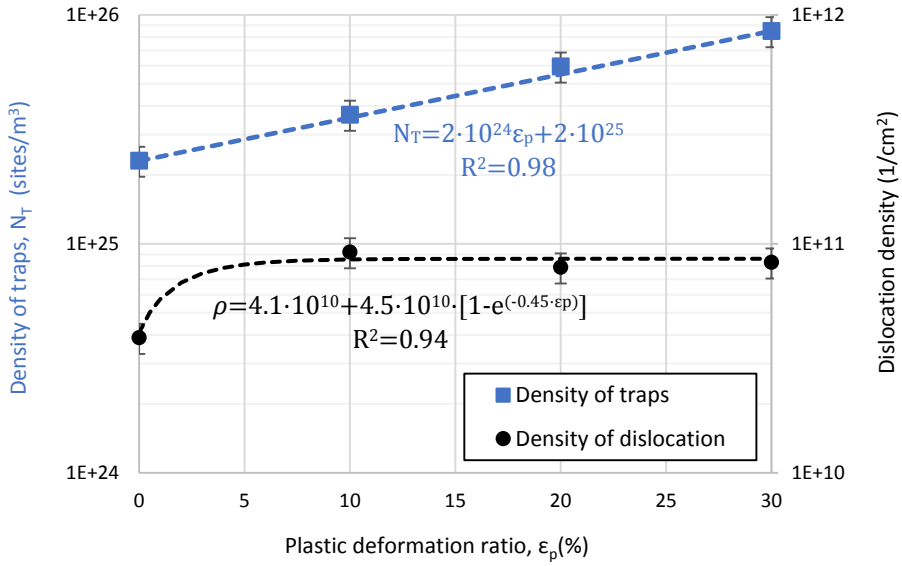


*Figure 18. Effect of the plastic deformation rate on the hydrogen trapping of the 2.25Cr1MoV steel grade*

Figure 19 shows the determined inverse relationship between density of traps ($N_T$) and the apparent diffusivity ($D_{app}$) as a function of the plastic deformation ratio in the V-added steel grade.

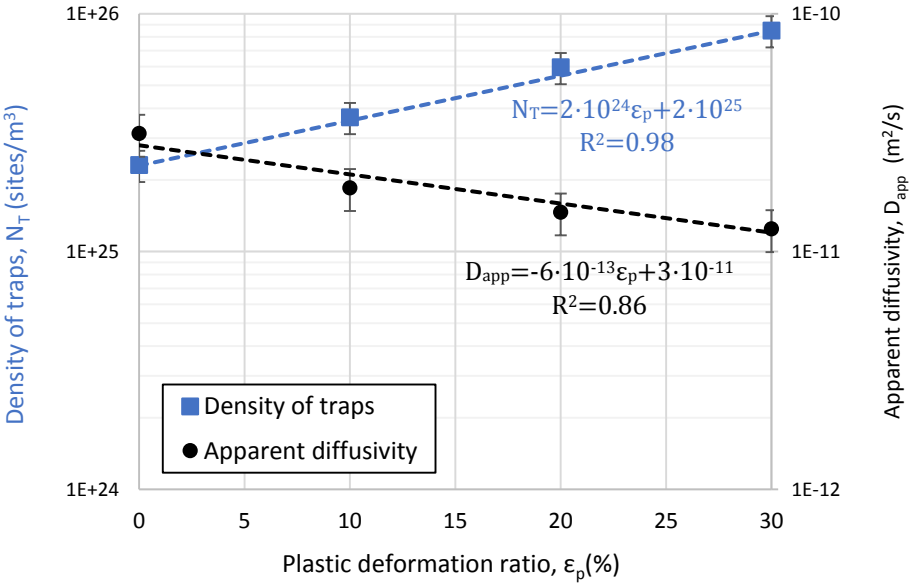


*Figure 19. Effect of the plastic deformation rate on the hydrogen diffusion kinetic of the 2.25Cr1MoV steel grade*

Hydrogen states estimated from the total decay after switching-off the cathodic current density are given in Table 9, while Figure 20 shows the ratios of each hydrogen state depending on the plastic deformation ratio.

| $\varepsilon_p$ (%) | $C_{Lattice}$ (ppm) | $C_{rev}$ (ppm) | $C_{irrev}$ (ppm) | $\Delta E_{TL}$ (eV) |
|---|---|---|---|---|
| 0 | 0.20 | 1.00 | 2.40 | 0.59 |
| 10 | 0.30 | 1.20 | 5.00 | 0.60 |
| 20 | 0.35 | 1.35 | 6.80 | |
| 30 | 0.40 | 1.60 | 8.00 | |

*Table 9. Hydrogen states in the 2.25Cr1MoV steel grade*

According to these results, the lattice hydrogen content ($C_{Lattice}$) and the reversible trapped hydrogen ($C_{rev}$) barely increased after the cold rolling process. However, irreversible trapped hydrogen content ($C_{irrev}$) notably increased from 2.40 ppm ($\varepsilon_p$=0%) to 8.00 ppm ($\varepsilon_p$=30%) as plastic deformation ratio increased (Figure 20). Although the estimated trapping energies in the range of 0.6eV (~58 kJ/mol) seem to be associated to dislocation core, it is well known that sub-micrometric vanadium carbides precipitated during the tempering treatments might also act as non-diffusible trapping sites [6, 7]. Hence, the interplay between dislocations and vanadium carbides (as strong trapping sites) contributes notably to the increase of the irreversible trapped hydrogen content.

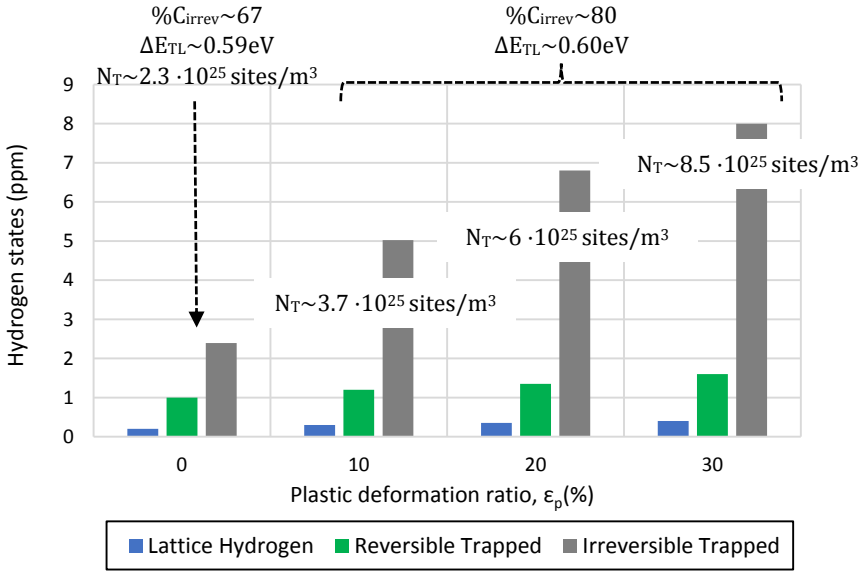


*Figure 20. Evolution of irreversible, reversible trapped and lattice hydrogen as a function of the plastic deformation ratio. 2.25Cr1MoV steel grade*

## 4 Discussion

Experimental results obtained from the hydrogen permeation tests, highlight that the microstructure and cold-work influenced the hydrogen diffusion and trapping processes. In order to discuss the hydrogen diffusion kinetics behavior observed in the 2.25Cr1Mo (V-free) and 2.25Cr1MoV (V-added) steel grades, thermal desorption analysis (TDA) analysis was also conducted. Therefore, hydrogen diffusion and trapping can be discussed on the basis of microstructural observations, results from TDA analysis and the aforementioned hydrogen electrochemical permeation tests. However, according to the results, some discrepancies between the detrapping activation energies estimated in permeation technique and TDA analysis were found. Regarding the TDA technique, the location and shape of TDA spectra seem to depend on the hydrogen distribution within the samples [52-54]. After the high-temperature charging in the high-pressure hydrogen reactor, final hydrogen distribution depends on the time elapsed between the end of high-temperature charging and the beginning of a temperature programmed ramp ($\phi_i$) in the TDA equipment. Here, after the maintenance time (21 hours in the high-pressure hydrogen reactor), a cooling phase of 1 hour, until a temperature of 85ºC was applied (for removing the pre-charged samples from the hydrogen reactor), as mentioned above. A consequence of this, part of hydrogen is released during the cooling phase (from 450 to 85ºC) and consequently, hydrogen distribution along the radial section of the cylindrical sample is not homogeneous [3]. This 'drawback' seems to affect TDA spectra [52] by altering the desorption peaks (compared to those that would be obtained with homogeneous distribution) what might contribute to explain the discrepancies found in the detrapping activation energies estimated from the permeation technique and from the TDA spectra, where the hydrogen desorption peak corresponding to dislocation core was not clearly identified. Consequently, further investigations must be carefully conducted to analyze the influence of the charging methodology in the TDA spectra.

Figure 21 gives the thermal desorption analysis of the studied grades of steel (un-deformed state) under the different heating rates ($\phi_i$). According to these results, Figure 22 shows the linear regressions applied to determine the detrapping activation energies ($\Delta E_{TL}$) corresponding to the different peaks identified in the 2.25Cr1Mo steel and also in the 2.25Cr1MoV steel grade. According to these results, Table 10 displays the slope, m, of the $\ln(\phi_i/T_{p_i}^2)$ versus $(1/T_{p_i})$ plots, the $R^2$ determination coefficient and the detrapping activation energy, '$\Delta E_{TL}$', calculated from TDA analysis performed on both steel grades (with and without vanadium). The excellent regressions obtained in all these analysis is worth noting, with determination coefficients, $R^2$, about 0.95-1.

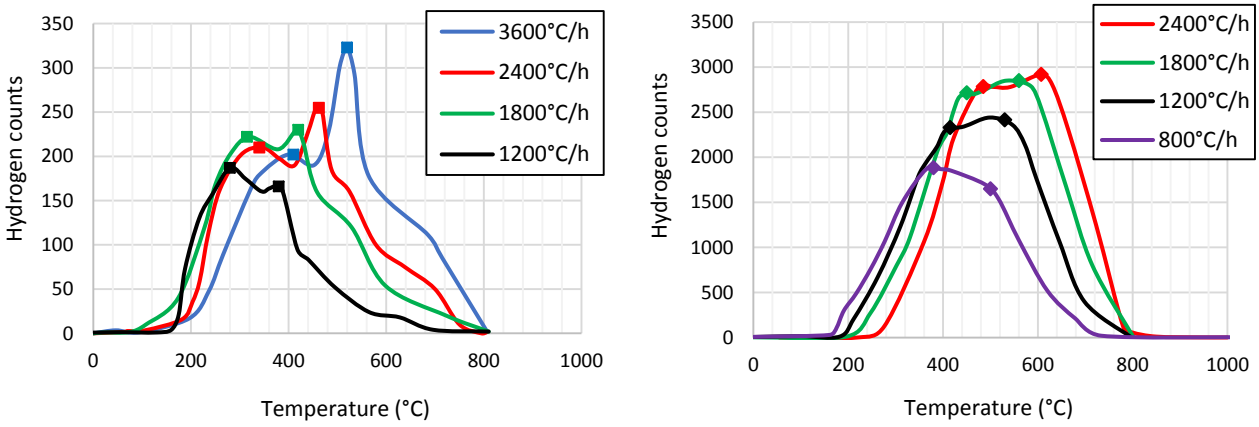


*(a)* *(b)*

*Figure 21. TDA spectra in the un-deformed state ($\varepsilon_p$=0%). (a) 2.25Cr1Mo and (b) 2.25Cr1MoV*

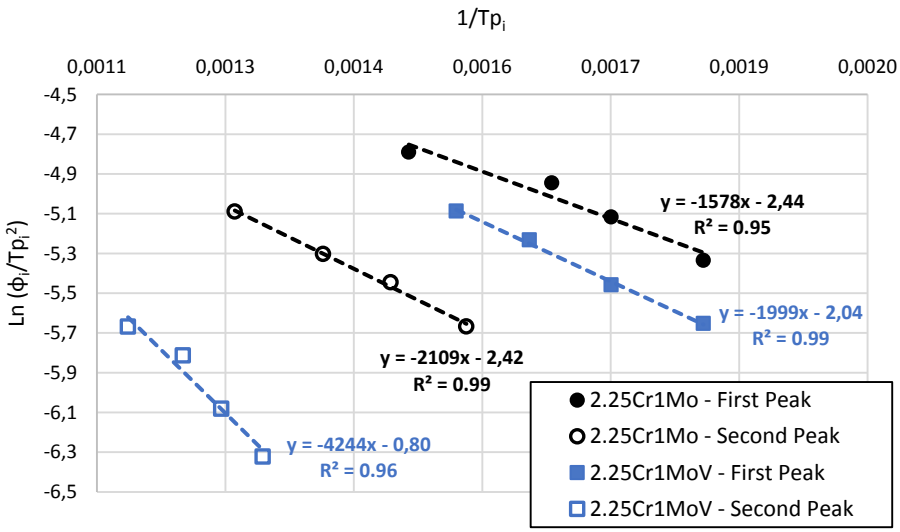


*Figure 22. Determination of detrapping activation energies on the 2.25Cr1Mo_ $\varepsilon_p$=0% and 2.25Cr1MoV_$\varepsilon_p$=0% steel grades according to TDA spectra (Figure 21).*

| Steel grade | TDA spectra | | | |
|---|---|---|---|---|
| | Position peak | m (slope) | $\Delta E_{TL}$ (kJ/mol) | $R^2$ |
| 2.25Cr1Mo ($\varepsilon_p$=0%) | 1st | 1578 | 13 | 0.95 |
| | 2nd | 2109 | 18 | 0.99 |
| 2.25Cr1MoV ($\varepsilon_p$=0%) | 1st | 1999 | 17 | 0.99 |
| | 2nd | 4244 | 35 | 0.96 |

*Table 10. Detrapping activation energies ($\Delta E_{TL}$ in kJ/mol)*

In the V-free steel grade (un-deformed state, $\varepsilon_p$=0%), two peaks were identified (Figure 21a). The detrapping activation energy determined for the first peak, ~13kJ/mol, has been associated with the ferrite/carbides interfaces [18, 55]. According to [20], this energy is associated to (Cr, Mo) carbides. Therefore, it is reasonable to consider that hydrogen atoms were reversibly trapped in Cr-Mo carbides which act as weak trap sites for hydrogen [20, 56]. The detrapping activation energy obtained for the second peak, ~18kJ/mol, was attributed to lath and packet martensite interfaces [18, 19] identified in Figure 7(a), which are considered as reversible traps for hydrogen.

Three preferential hydrogen trapping sites have been identified in the V-free steel grade: dislocation core (55-60kJ/mol), Cr-Mo carbides (13kJ/mol) and martensite interfaces

(18kJ/mol). Therefore, our initial hypothesis, that dislocation core was considered as the main type of hydrogen trapping site, is now confirmed by comparing its very strong hydrogen binding energy to the other microstructural trapping sites (Cr/Mo carbides and martensite interfaces).

It is important to remember that the main difference between 2.25Cr1Mo steel grade (V-free) and 2.25Cr1MoV steel grade (V-added) was the vanadium addition (+0.31%). Hence, the addition of vanadium to chromium-molybdenum steel promoted precipitation of mixed vanadium-molybdenum sub-micrometric carbides, MC (Figure 23).

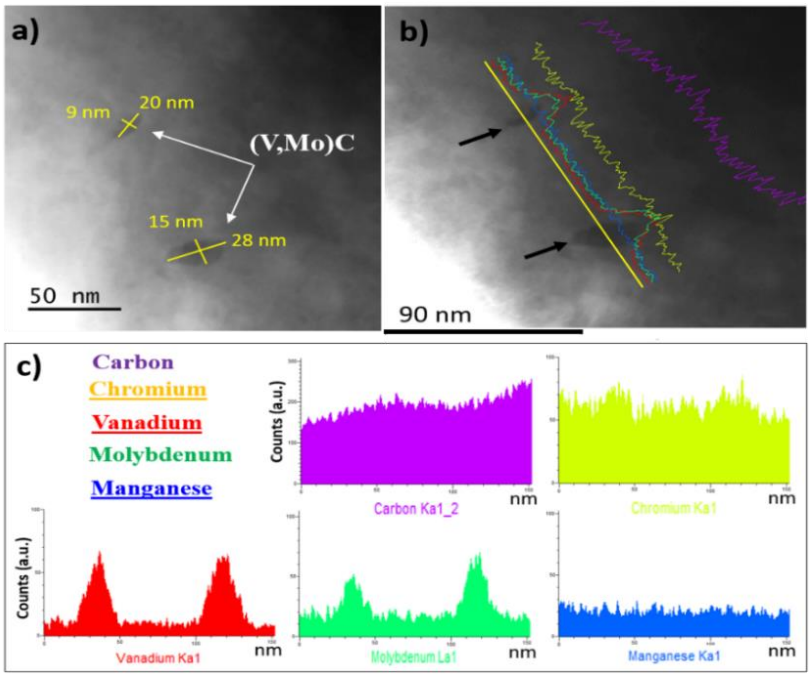


*Figure 23. TEM Analysis of V-added grade. (a,b) STEM images; the yellow line in (b) shows element line-scan profiles for C (purple), Cr (lime), V (red), Mo (green) and Mn (blue). (c) Line-scan plots of number of counts versus distance recorded along the yellow line shown in the image (b).*

According to this, in the 2.25Cr1MoV steel grade, the second peak (Figure 21b), with the highest detrapping activation energy around 35 kJ/mol is the activation energy of hydrogen desorption from vanadium carbides, and agreed well with the previous works of Asahi et al. [6] and Yamasaki et al. [7]. Thus, the contribution on hydrogen trapping of another type of microstructural trap (MC carbides) is now confirmed. On the other hand, the first peak with a detrapping activation energy around 17 kJ/mol was also associated to lath and packet martensite interfaces [18, 19].

The identified hydrogen desorption peaks were shifted to a higher temperature than the V-free steel grade, as shown in Figure 24. This phenomenon, also observed by other authors [57], can be ascribed to the vanadium carbides effect (which act as strong traps for hydrogen) by comparing TDA peaks of un-deformed V-free and un-deformed V-added steel grades. This supports the results obtained in the hydrogen permeation tests, (Figure 25), where vanadium addition (+0.31%) notably contributed to delay hydrogen permeation kinetic within the steel microstructure.

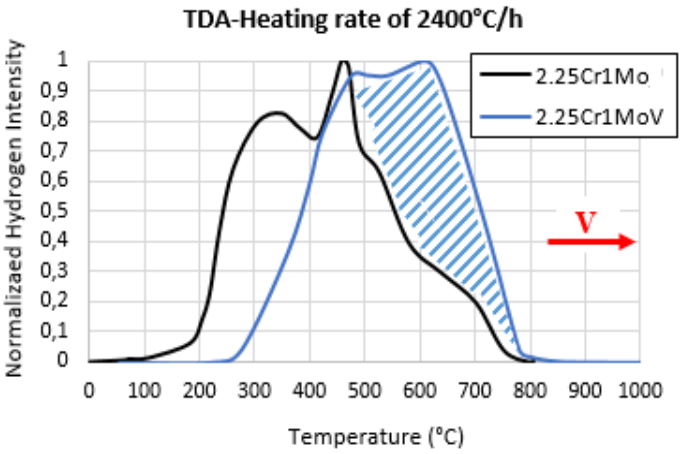


*Figure 24. Vanadium contribution in hydrogen desorption (MC carbides)*

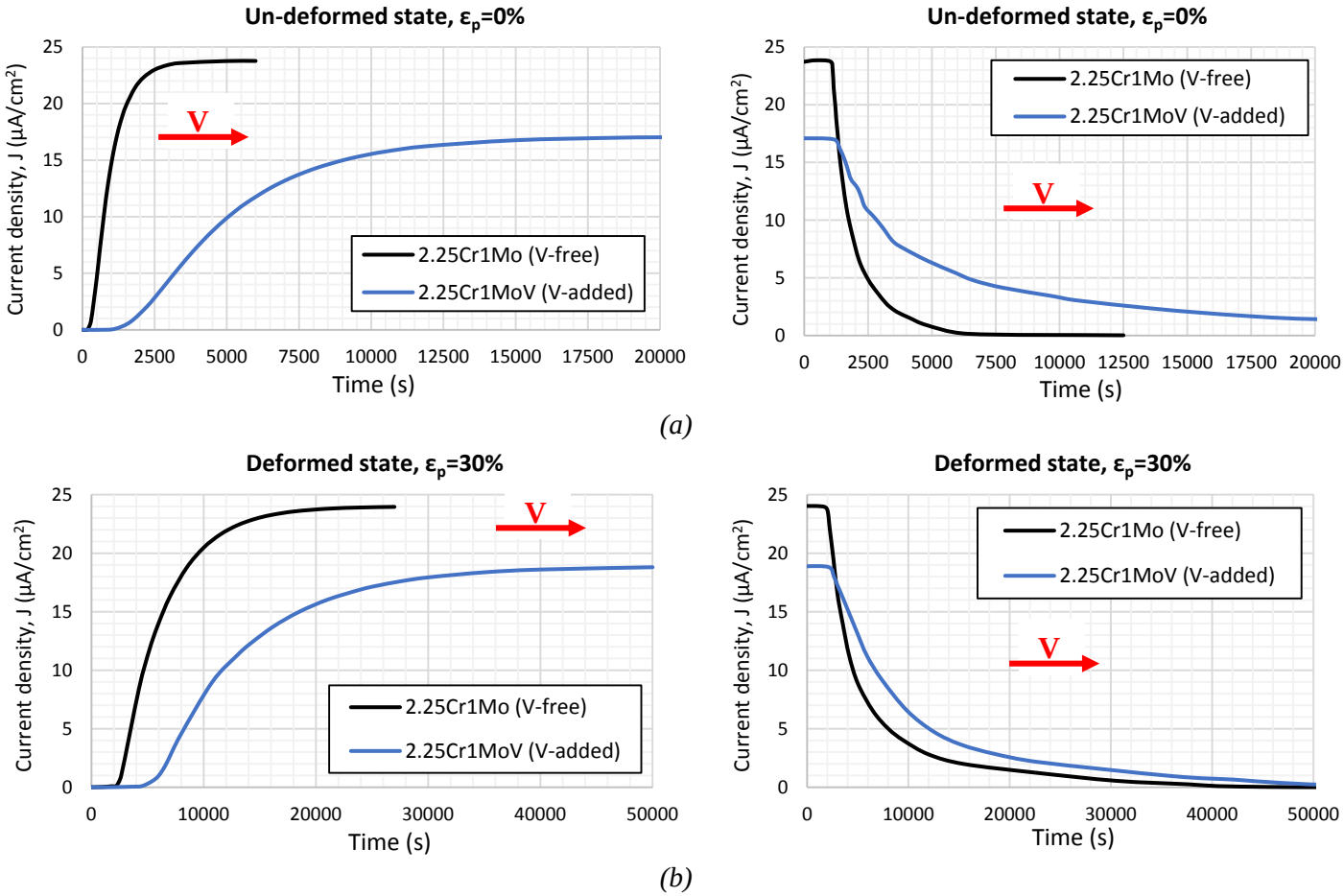


*Figure 25. Vanadium contribution on hydrogen permeation. (a) Without plastic deformation ($\varepsilon_p$=0%) and (b) after 30% of `plastic deformation ratio ($\varepsilon_p$=30%)*

Hence, the apparent diffusion coefficient ($D_{app}$) determined in the V-added grade with different plastic deformation ratios was always lower than that calculated one for the V-free steel grade (Figure 26a). For example, when both steels are compared in the un-deformed steel, the apparent diffusion coefficient ($D_{app}$) determined in the V-free grade was five times higher than the one estimated for the V-added steel grade. This fact is explained due to the higher density of total traps estimated in the V-added steel grade

(Figure 26b). In addition, although dislocation core was identified on both grades of steel as the strongest trapping sites (with $\Delta E_{TL}$~55-60 kJ/mol), precipitated vanadium carbides (MC submicrometric carbides in the V-added steel, Figure 23) with an activation energy around 35 kJ/mol (well above activation energy for desorption from Fe-Cr-Mo carbides, ~13 kJ/mol) also explain the slower hydrogen diffusion kinetics determined in the V-added grade. Due to the V-addition, hydrogen trapping was more notable (Figure 26c).

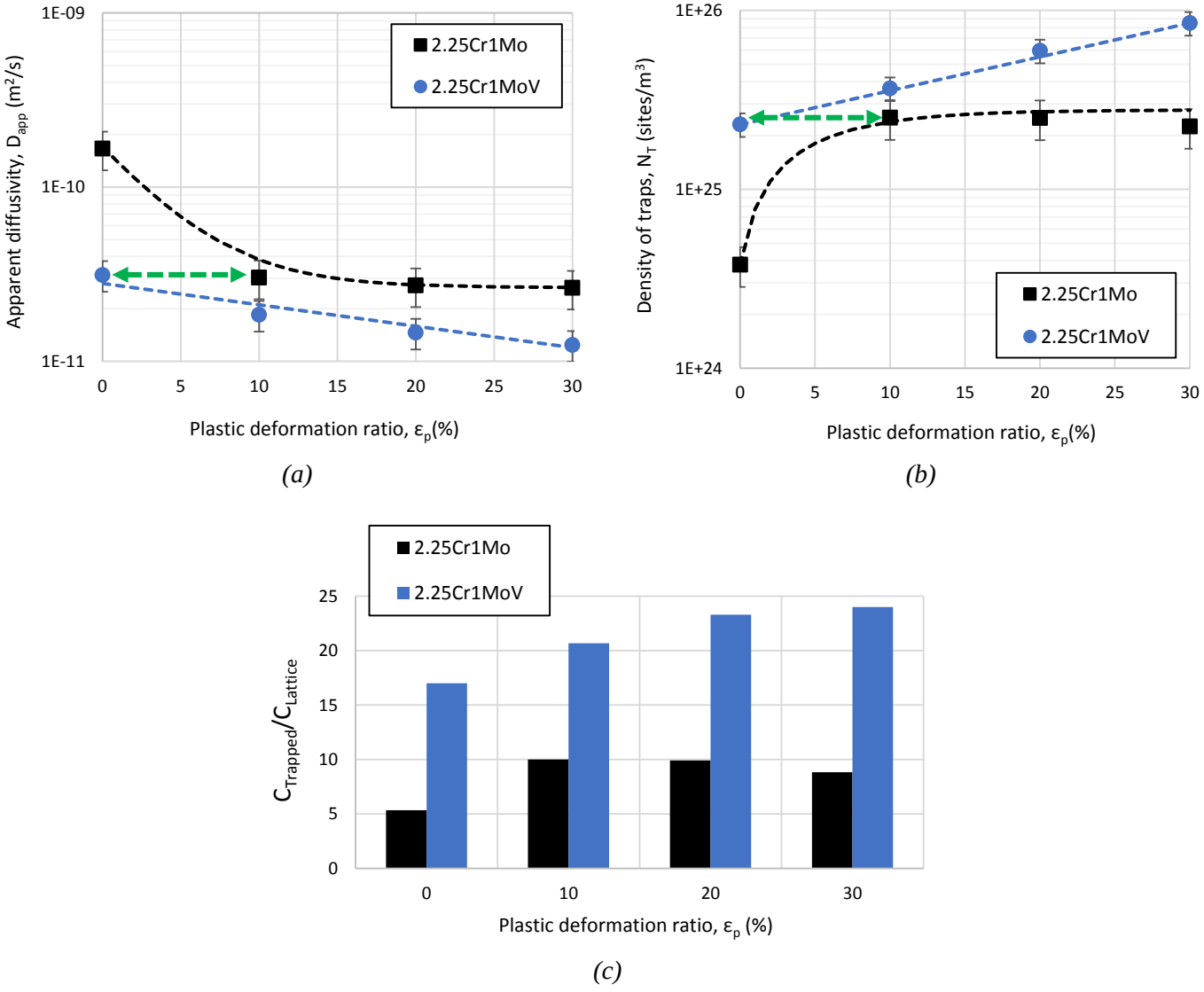


*Figure 26. Plastic deformation ratio influence in the apparent hydrogen diffusivity (a), trapping sites density (b) and $C_{Trapped}/C_{Lattice}$ ratio (c) with $C_{Trapped}=C_{rev}+C_{irrev}$*

On the other hand, it is important to mention that cold-worked V-free grade in the $\varepsilon_p$=10% -state exhibited similar hydrogen diffusion kinetics to that observed in the un-deformed ($\varepsilon_p$=0%) V-added steel grade (Figure 26a, green arrow). In the V-free grade, the density of traps increased up to $2.52 \cdot 10^{25}$ sites/$m^3$ when 10% of plastic deformation was applied. In this case, the estimated dislocation density was around $5.9 \cdot 10^{10}$ 1/$cm^2$ (after cold-work). However, in the un-deformed V-added grade, cold-work was not required to achieve a similar total trapping density, $2.3 \cdot 10^{25}$ sites/$m^3$ (Figure 26b, green arrow), although dislocation density was around 30% lower ($\rho$ =$3.9 \cdot 10^{10}$ 1/$cm^2$). This fact is

adscribed to the presence of the aforementioned sub-micrometric vanadium carbides (MC) that act as strong traps for hydrogen, thus contributing to increase the density of total trapping sites. According to this behavior, the apparent diffusion coefficient ($D_{app}$) determined in both cases ($\varepsilon_p$=10% V-free and $\varepsilon_p$=0% V-added steel) was very similar, e.g. around $3 \cdot 10^{-11}$ $m^2/s$.

According to the employed techniques, dislocations core was identified as the strongest trapping sites on both grades of steel in view of its strong hydrogen detrapping activation energy ($\Delta E_{TL}$~55-60kJ/mol). On the other hand, martensite interfaces was also identified as trapping sites ($\Delta E_{TL}$~17-18 kJ/mol in both steel grades). Nevertheless, the main difference between the two steel grades was the activation energy value for hydrogen desorption from carbides. Indeed, sub-micrometric vanadium carbides were identified with an activation energy ~35 kJ/mol (in the V-added grade) well above activation energy for hydrogen detrapping from Cr-Mo carbides (~13 kJ/mol in the V-free grade). Identified trapping sites are shown in Figure 27.

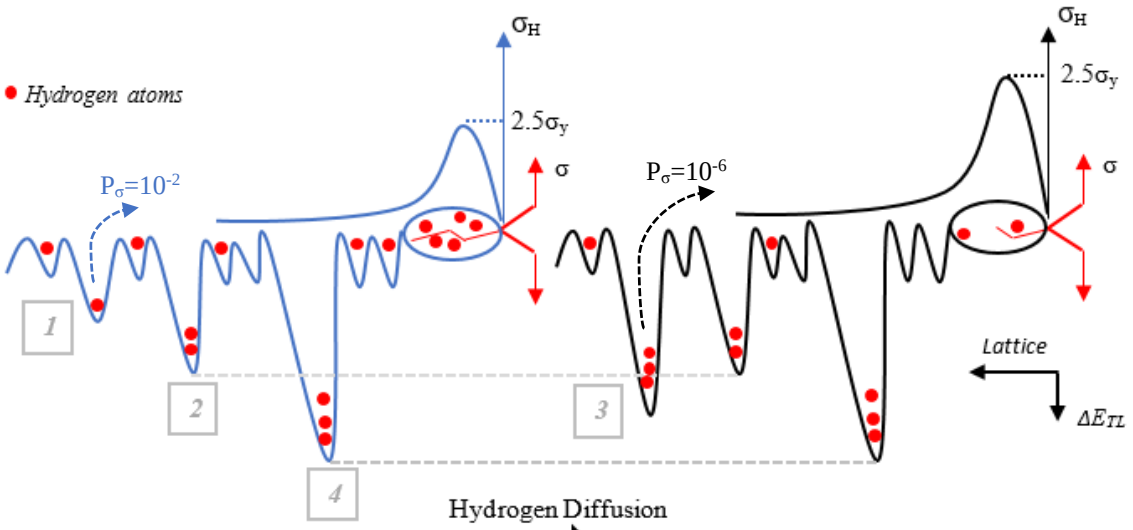


| Region | $\Delta E_{TL}$(kJ/mol) | Trapping site |
|---|---|---|
| 1 | 13 | (Cr-Mo)C |
| 2 | 17-18 | Martensite interfaces |
| 3 | 35 | (Mo-V)C |
| 4 | 55-60 | Dislocation core |

*Figure 27. Identified trapping sites in 2.25Cr1Mo(V) steel grades. Hydrogen diffusion towards the stress concentrator near the notch area*

The equilibrium probability ($P_\sigma$) of hydrogen repartitioning from traps (detrapping) to the crack tip (illustrated in Figure 27) under tensile hydrostatic stress ($\sigma_H$) is given by equation 25 [58], where: '$V_H$' is the partial molar volume of hydrogen in BCC Fe ($2.1 \cdot 10^{-6}$ $m^3/mol$), 'R' is the gas constant, 'T' is the temperature and '$\Delta E_{TL}$' is the hydrogen detrapping activation energy.

$$P_\sigma = \frac{\exp\left(\frac{\sigma_H \cdot V_H}{R \cdot T}\right)}{\exp\left(\frac{\sigma_H \cdot V_H}{R \cdot T}\right) + \exp\left(\frac{\Delta E_{TL}}{R \cdot T}\right)} \qquad (25)$$

Classical continuum fracture mechanics suggests that $\sigma_H$ is $2.5\sigma_y$ for a low strain hardening [59]. Therefore, detrapping probability ($P_\sigma$) associated with a specific trapping site can be estimated. Accordingly, the probability of hydrogen repartitioning to the crack tip in the V-free steel is $10^{-2}$ assuming detrapping from Cr-Mo carbides while, in the V-added is very low, around $10^{-6}$ assuming detrapping from mixed Mo-V carbides (Figure 27). Hence, precipitated sub-micrometric Mo-V carbides contribute to prevent hydrogen diffusion towards the damage process zone (crack tip). Therefore, hydrogen accumulation on the process zone is limited, contributing to improve the steel behavior under hydrogen environments [3, 5, 60].

## 5 Conclusions

This work evaluated hydrogen trapping and diffusion kinetics of 2.25Cr1Mo(V) steel grades subjected to different cold-plastic deformation ratios. Based on the results from a wide experimental campaign, these conclusions can be drawn:

- Plastic deformation, induced by means of cold-rolling process, contributes to delay the hydrogen diffusion kinetics, mainly thanks to the increase in the density of traps (i.e. dislocations density). However, the steady-state hydrogen current density remains unaffected, independently on the applied plastic deformation ratio.
- In the 2.25Cr1Mo steel, hydrogen apparent diffusion coefficient decreased after the cold-work due to the increase in the density of traps. However, after 10% of plastic deformation, apparent diffusion coefficient 'saturates', following the trend marked by the dislocation density evolution. Lattice diffusivity was also influenced by the cold-work.
- Although dislocation core (with $\Delta E_{TL}$~55-60kJ/mol) was identified as the main trapping sites in the 2.25Cr1Mo steel grade, martensite interfaces (18kJ/mol) and mixed Fe-Cr-Mo carbides (13kJ/mol) are also involved in the trapping phenomena.
- Due to the vanadium addition (+0.31%), hydrogen apparent diffusion coefficient was notably reduced (compared to that obtained in the V-free steel grade). Hydrogen trapping and diffusion are the result of the interplay between vanadium carbides (35kJ/mol) and dislocations.
- Cold-worked 2.25Cr1Mo steel grade in the $\varepsilon_p$=10%-deformed state ($\rho = 5.9 \cdot 10^{10}$ 1/cm$^2$) exhibited hydrogen diffusion kinetics similar to the un-deformed ($\varepsilon_p$=0%) 2.25Cr1MoV steel grade ($\rho = 3.9 \cdot 10^{10}$ 1/cm$^2$). This fact highlights the important role that vanadium carbides (MC) play on hydrogen trapping.
- 2.25Cr1MoV steel grade constitutes a good manufacturing option for industrial components of high-pressure hydrogen gas. Precipitated vanadium carbides during tempering treatments act as strong traps for hydrogen, reducing the hydrogen detrapping probability (compared to that estimated in the V-free steel grade). This contributes to limit hydrogen accumulation in the crack-tip region, susceptible to hydrogen embrittlement.

**Acknowledgments**

The authors would like to thank financial aid given by FEDER, the Asturias government, through the project FC-GRUPIN-IDI/2018/0001341 and Spanish MINECO (MAT2016-78155C2-1-R).

**References**

[1] R.P.Gangloff , B.P.Sommerday. 'Gaseous hydrogen embrittlement of materials in energy technologies'. Volume 1: The problem, its characterisation and effects on particular alloy classes. Woodhead Publishing, 2012.

[2] A.Oudriss, A.Fleurentin, G.Courlit, E.Conforto, C.Berziou, C.Rébéré, S.Cohendoz, J.M.Sobrino, J.Creus, X.Feaugas. 'Consequence of the diffusive hydrogen contents on tensile properties of martensitic steel during the desorption at room temperature'. Materials Science Engineering A, Volume 598, 2014, 420-428.

[3] L.B.Peral, A.Zafra, S.Blasón, C.Rodríguez, J.Belzunce. 'Effect of hydrogen on the fatigue crack growth rate of quenched and tempered CrMo and CrMoV steels'. International Journal of Fatigue, Volume 120, 2019, 201-214.

[4] S. Frappart, A.Oudriss, X. Feaugas, J. Creus, J.Bouhattate, F.Thébault, L. Delattre, H.Marchebois. 'Hydrogen trapping in martensitic steel investigated using electrochemical permeation and thermal desorption spectroscopy'. Scripta Materialia, Volume 65, 2011, 859-862.

[5] L.B.Peral. A.Zafra, I.Fernández-Pariente, C.Rodríguez and J.Belzunce. 'Effect of Internal Hydrogen on the Tensile Properties of Different CrMo(V) steel grades: Influence of Vanadium Addition on Hydrogen Trapping and Diffusion'. Volume 45, Issue 21, 2020, 22054-22079.

[6] H.Asahi, D.Hirakami, S.Yamasaki. 'Hydrogen trapping behavior in vanadium-added steels'. ISIJ International, Volume 43, Issue 4, 2003, 527-533.

[7] S. Yamasaki, T. Takahashi, 'Evaluation method of delayed fracture property of high strength steels'. Tetsu-to-Hagane, 83, 1997, 454-459.

[8] H.G.Lee, Jai-Young Lee. 'Hydrogen trapping by TiC particles in iron'. Acta Metallurgica, Volume 32, Issue 1, 1984, 131-136.

[9] I.Maroef, D.L.Olson, M.Eberhart, G.R.Edwards. 'Hydrogen trapping in ferritic steel weld metal', International Materials Reviews, Volume 47, Issue 4, 2012, 191-223.

[10] J.Y.Lee and J.L. Lee. 'A trapping theory of hydrogen in pure iron'. Philosophical Magazine A, Volume 57, Issue 3, 1987, 293-309.

[11] M.Nagumo, M.Nakamura and K.Takai. 'Hydrogen thermal desorption relevant to delayed-fracture susceptibility of high-strength steels'. Metallurgical and Materials Transactions A, Volume 32, 2001, 339-347.

[12] L.Jemblie, V.Olden, O.M.Akselsen. 'A couple diffusion and cohesive zone modelling approach for numerically assessing hydrogen embrittlement of steel structures', International Journal of Hydrogen Energy, Volume 42, Issue 16, 2017, 11980-11995.

[13] H.K.D.H. Badeshia. 'Prevention of hydrogen embrittlement in steels', ISIJ International, Volume 56, Issue 1, 2016, 24-36.

[14] S. Frappart, J. Creus, L. Delattre, X. Feaugas, F. Thebault, H. Marchebois. 'Study of the hydrogen diffusion and segregation into Fe-C-Mo martensitic HSLA steel using electrochemical permeation test'. Journal of Physics and Chemistry of Solids, Volume 71, Issue 10, 2010, 1467-1479

[15] A.Ramasubramanian, M.Itakura, E.A.Carter. 'Interatomic potentials for hydrogen in α-iron based on density functional theory'. Physical Review B, 2009, 1-13.

[16] R G.L.Spencer, D.J.Duquette. 'The role of vanadium carbide traps in reducing the hydrogen embrittlement susceptibility of high strength alloy steels'. Technical report ARCBB-TR-98016, US Army Armament Research, N.Y. 1998.

[17] Ji Soo Kim, You Hwan Lee, Duk Lak Lee, Kyung-Tae Park, Chong Soo Lee. 'Microstructural influences on hydrogen delayed fracture of high strength steels'. Materials Science and Engineering: A, Volume 505, Issues 1-2, 2009, 105-110

[18] G.W.Hong, J.Y.Lee. 'The measurement of the trap binding energy by the thermal analysis technique'. Scripta Metallurgica, Volume 17, Issue 7, 1983, 823-826.

[19] K.Takasawa, R.Ishigaki, Y.Wada, R.Kayano. 'Absorption of hydrogen in high-strength low-alloy steel during tensile deformation in gaseous hydrogen'. ISIJ International, Volume 97, Issue 5, 2011, 288-294

[20] H.Dogan, D.Li and J.R.Scully. 'Controlling Hydrogen Embrittlement in Precharged Ultrahigh-Strength Steels'. Corrosion Science, Volume 63, Issue 7, 2007, 689-703.

[21] V.P.Ramuni, R.C.Paisanot, P.Bruzzoni. 'Search of hydrogen transition states on α-Fe: The monometer adapted to first principles calculations'. Physica B, Volume 404, 2009, 2880-2882.

[22] A.Díaz, J.M.Alegre, I.I.Cuesta. 'Numerical simulation of hydrogen embrittlement and local triaxiality effects in notched specimens'. Theoretical and Applied Fracture Mechanics, Volume 90, 2017, 294-302.

[23] G.Álvarez, A.Zafra, F.J.Belzunce, C.Rodríguez. 'Hydrogen embrittlement in a CrMoV steel by means of sent specimens'. Theoretical and Applied Fracture Mechanics, Volume 106, 2020, 102450.

[24] G.Álvarez, L.B.Peral, C.Rodríguez, T.E.García, F.J.Belzunce. 'Hydrogen embrittlement of structural steels: Effect of displacement on the fracture toughness of high-pressure hydrogen pre-charged samples'. International Journal of Hydrogen Energy, Volume 44, Issue 29, 2019, 15364-15643.

[25] R.A.Oriani, P.H.Josephic. 'Effects of Hydrogen on the plastic properties of medium-Carbon steels'. Metallurgical Transactions A, Volume 11, 1980, 1809-1820

[26] M.E.Fitzpatrick. 'Determination of Residual Stresses by X-ray Diffraction'. Measurement Good Practice Guide No 52. Issue 2, 2005.

[27] G.K.Williamson, W.H.Hall. 'X-Ray line broadening from filed aluminium and wolfram'. Acta Metallurgica, Volume 1, Issue 1, 1953, 22-31.

[28] H.P. Klug, L.E. Alexander, 'X-ray Diffraction Procedures', John Wiley & Sons, New York, 1954

[29] G.K Williamson, R.E Smallman. 'Dislocation densities in some annealed and cold worked metals from measurements on the X-ray debye-scherrer spectrum'. Philosophical Magazine: A Journal of Theoretical Experimental and Applied Physics, Volume 1, 1956, 34-46

[30] M.N.Yoozbashi, S.Yazdani. 'XRD and TEM study of bainitic ferrite plate thickness in nanostructured, carbide free bainitic steels'. Materials Chemistry and Physics, Volume 160, 2015, 148-154.

[31] M.A.V.Devanathan, Z.Stachursky. 'The Adsorption and Diffusion of Electrolytic Hydrogen in Palladium'. Proceedings of the Royal Society of London. Series A, Mathematical and Physical Sciences, Volume 270, Issue 1340, 1962, 90-102.

[32] H.El Alami, J.Creus, X.Feaugas. 'Influence of the plastic strain on the hydrogen evolution reaction on polycrystalline nickel electrodes in $H_2SO_4$'. Electrochimica Acta, Volume 51, Issue 22, 2006, 4716-4727.

[33] P. Manolatos, M. Jerome, J. Galland. 'Necessity of a Palladium coating to ensure hydrogen oxidation during electrochemical permeation measurements on iron'. Electrochimica Acta 40, 1995, 867-871

[34] S. Serna, H. Martínez, S.Y. López, J.G Gonzalez-Rodriguez, J.L. Albarrán. 'Electrochemical technique applied to evaluate hydrogen permeability in microalloyed steels'. International Journal of Hydrogen Energy, 30, 2005, 1333-1338.

[35] ASTM G148-97. 'Standard practice for evaluation of hydrogen uptake, permeation and transport in metals by an electrochemical technique', 2011.

[36] S. Frappart, J. Creus, L. Delattre, X. Feaugas, F. Thebault, H. Marchebois. 'Study of the hydrogen diffusion and segregation into Fe-C-Mo martensitic HSLA steel using electrochemical permeation test'. Journal of Physics and Chemistry of Solids, Volume 71, Issue 10, 2010, 1467-1479.

[37] A. McNabb, P.K.Foster. 'A new analysis of the diffusion of hydrogen in iron and ferritic steels'. Trans. Met. Soc. AIME, 27, 1963, 618-627.

[38] A.J. Kumnick, H.H. Johnson. 'Deep trapping states for hydrogen in deformed iron'. Acta Metallurgica, 28, 1980, 33-39.

[39] T. Zakroczymski. 'Adaptation of the electrochemical permeation technique for studying entry, transport and trapping of hydrogen in metals'. Electrochimica Acta, Volume 51, Issue 11, 2006, 2261-2266.

[40] E. Fallahmohammadi, F. Bolzoni, L. Lazzari. 'Measurement of lattice and apparent diffusion coefficient of hydrogen in X65 and F22 pipeline steels'. International Journal of Hydrogen Energy, 38, 2013, 2531-2543.

[41] R.A. Oriani. 'The diffusion and trapping of hydrogen in steel'. Acta Metallurgica, Volume 18, Issue 1, 1970, 147-157.

[42] A.H.M Krom, A.D. Bakker. 'Hydrogen trapping models in steel'. Metallurgical and Materials Transactions B, Volume 31, 2000, 1475-1482.

[43] D.F.Araujo, E.O.Villar, J.Palma Carrasco. 'A critical review of mathematical models used to determine the density of hydrogen trapping sites in steel and alloys'. International Journal of Hydrogen Energy, Volume 39, 2014, 12194-12200.

[44] ASTM G146. 'Evaluation of disbonding of bimetallic stainless alloy/steel plate for use in high pressure, high temperature refinery hydrogen service'. In: Annual Book of ASTM Standards, vol. 03.02; 2013.

[45] Kissinger HE. 'Reaction kinetics in different thermal analysis'. Analytical Chemistry, Volume 29, 1957, 1702-1706.

[46] P.Castaño-Rivera, V.P.Ramunni, P.Bruzzoni. 'Hydrogen Trapping in an API 5L X60 Steel'. Corrosion Science, Volume 54, 2012, 106-118.

[47] W.Dietzel, M.Pfuff, G.G.Juilfs. 'Hydrogen Permeation in Plastically Deformed Steel Membranes'. Materials Science, Volume 42, 2006, 78-84.

[48] K.Kiuchi, R.B.McLellan, 'The solubility and diffusivity of hydrogen in well-annealed and deformed iron'. Acta Metallurgica, Volume 31, Issue 7, 1983, 961-984.

[49] H.J.Grabke, E.Riecke. 'Absorption and diffusion of hydrogen in steels'. Materials Technology, Volume 34, 2000, 331-342.

[50] E. Fallahmohammadi, R. Ballinger, Y. Maruno, G. Fumagalli, G. Re, L. Lazzari. 'Effect of Plastic Deformation on Hydrogen Diffusion of X65 Pipeline Steel'. In Proceedings of the NACE-International Corrosion Conference Series, San Antonio, Texas, USA, 9-13 March 2014.

[51] D.E.Jiang, E.A.Carter. 'Diffusion of interstitial hydrogen into and through bcc Fe from first principles'. Physical Review B 70, Volume 70, 2004, 1-9.

[52] Hurley C, Martin F, Marchetti L, Chêne J, Blanc C, Andrieu E. 'Numerical modelling of thermal desorption mass spectroscopy (TDS) for the study of hydrogen diffusion and trapping interactions in metals', International Journal of Hydrogen Energy, Volume 40, 2015, 3402-3414.

[53] A. Díaz, I.I.Cuesta, E. Martínez-Pañeda, J.M.Alegre. 'Influence of charging conditions on simulated temperature-programmed desorption for hydrogen in metals'. International Journal of Hydrogen Energy, Volume 45, Issue 43, 2020, 23704-23720

[54] E. Legrand, A. Oudriss, C. Savall, J. Bouhattate, X. Feaugas. 'Towards a better understanding of hydrogen measurements obtained by thermal desorption spectroscopy

using FEM modeling'. International Journal of Hydrogen Energy, Volume 40, Issue 6, 2015, 2871-2881.

[55] D.G.Enos, J.R.Scully. 'A critical-strain criterion for hydrogen embrittlement of cold-drawn, ultrafine pearlitic steel'. Metallurgical and Materials Transactions A, Volume 33, 2002, 1151-1166.

[56] R.Valentini, A.Solina. 'Influence of microstructure on hydrogen embrittlement behaviour of 2.25Cr1Mo steel'. Materials Science and Technology, Volume 10, 1994, 908.

[57] T.Yokota, T.Shiraga, 'Evaluation of hydrogen content trapped by vanadium precipitates in a steel'. ISIJ International, Volume 43, Issue 4, 2003, 534-538.

[58] T.Y. Zhang, J.E. Hack. 'The equilibrium concentration of hydrogen atoms ahead of a mixed mode I-Mode III crack tip in single crystal iron'. Metallurgical and Materials Transactions A, Volume 30, 1999, 155-159.

[59] T.L Anderson. 'Fracture mechanics'. Fundamentals and Applications. Third edition, Taylor and Francis, 2005, USA

[60] L.B.Peral, A.Zafra, J.Belzunce, C.Rodríguez. 'Effects of hydrogen on the fracture toughness of CrMo and CrMoV steels quenched and tempered at different temperatures'. International Journal of Hydrogen Energy, Volume 44, Issue 7, 2019, 3953-3965.